The Sloan Digital Sky Survey *u*-band Galaxy Survey: luminosity functions and evolution

I. K. Baldry,[1][*] K. Glazebrook,[1] T. Budavári,[1] D. J. Eisenstein,[2] J. Annis,[3]
N. A. Bahcall,[4] M. R. Blanton,[5] J. Brinkmann,[6] I. Csabai,[1,7] T. M. Heckman,[1]
H. Lin,[3] J. Loveday,[8] R. C. Nichol[9] and D. P. Schneider[10]

[1]*Department of Physics and Astronomy, Johns Hopkins University, 3400 North Charles Street, Baltimore, MD 21218, USA*

[2]*Steward Observatory, 933 North Cherry Avenue, Tucson, AZ 85721, USA*

[3]*Fermi National Accelerator Laboratory, PO Box 500, Batavia, IL 60510, USA*

[4]*Department of Astrophysical Sciences, Princeton University, Princeton, NJ 08544, USA*

[5]*Center for Cosmology and Particle Physics, Department of Physics, New York University, 4 Washington Place, NY 10003, USA*

[6]*Apache Point Observatory, PO Box 59, Sunspot, NM 88349, USA*

[7]*Department of Physics of Complex Systems, Eötvös Loránd University, Pf. 32, H-1518 Budapest, Hungary*

[8]*Astronomy Centre, University of Sussex, Falmer, Brighton, BN1 9QJ*

[9]*Institute of Cosmology and Gravitation, Mercantile House, Hampshire Terrace, University of Portsmouth, Portsmouth PO1 2EG*

[10]*Department of Astronomy and Astrophysics, 525 Davey Laboratory, Pennsylvania State University, PA 16802, USA*

ABSTRACT

We construct and analyse a *u*-band selected galaxy sample from the Sloan Digital Sky Survey (SDSS) Southern Survey, which covers 275 deg^2. The sample includes 43 223 galaxies with spectroscopic redshifts in the range $0.005 < z < 0.3$ and with $14.5 < u < 20.5$. The signal-to-noise (S/N) ratio in the *u*-band Petrosian aperture is improved by co-adding multiple epochs of imaging data and by including sky-subtraction corrections. Luminosity functions for the near-UV $^{0.1}u$ band ($\lambda \approx 322 \pm 26$ nm) are determined in redshift slices of width 0.02, which show a highly significant evolution in M^* of -0.8 ± 0.1 mag between $z = 0$ and 0.3; with $M^* - 5 \log h_{70} = -18.84 \pm 0.05$ (AB mag), $\log \phi^* = -2.06 \pm 0.03$ (h_{70}^3 Mpc^{-3}) and $\log \rho_{\rm L} = 19.11 \pm 0.02$ (h_{70} W Hz^{-1} Mpc^{-3}) at $z = 0.1$. The faint-end slope determined for $z < 0.06$ is given by $\alpha = -1.05 \pm 0.08$. This is in agreement with recent determinations from the *Galaxy Evolution Explorer* at shorter wavelengths. Comparing our $z < 0.3$ luminosity density measurements with $0.2 < z < 1.2$ from Classifying Objects by Medium Band Observations in 17 Filters (COMBO-17), we find that the 280-nm density evolves as $\rho_{\rm L} \propto (1 + z)^{\beta}$ with $\beta = 2.1 \pm 0.2$; and find no evidence for any change in slope over this redshift range. By comparing with other measurements of cosmic star formation history, we estimate that the effective dust attenuation at 280 nm has increased by 0.8 ± 0.3 mag between $z = 0$ and 1.

Key words: surveys – galaxies: evolution – galaxies: fundamental parameters – galaxies: luminosity function, mass function – ultraviolet: galaxies.

1 INTRODUCTION

In the absence of dust, the rest-frame ultraviolet (UV) luminosity of a galaxy is nearly proportional to the total mass of short-lived OB stars and therefore to the star formation rate (SFR). This has been used to show that the volume-averaged SFR of the Universe has been declining since at least $z \sim 1$ (Lilly et al. 1996; Madau et al. 1996; Madau, Pozzetti & Dickinson 1998; Cowie, Songaila & Barger 1999; Steidel et al. 1999; Wilson et al. 2002). Until the

observations of the *Galaxy Evolution Explorer (GALEX)* (Martin et al. 2005), the accuracy in the measured evolution rate had been low because of the lack of 100–300 nm surveys at low redshift. The FOCA balloon-borne telescope (Milliard et al. 1992) had been the only instrument for measuring the galaxy luminosity function (LF) at these wavelengths; this survey covered about 2 deg^2 (Treyer et al. 1998; Sullivan et al. 2000). However, 'sun-tanning bands' $u/U/U'$ also provide a window on the star-forming properties of galaxies as they are significantly more sensitive to young stellar populations than the $B/b_J/g$ bands; over 5000 deg^2 has been imaged in the *u* band as part of the Sloan Digital Sky Survey (SDSS). Using these data, Hopkins et al. (2003) have demonstrated that the *u*-band
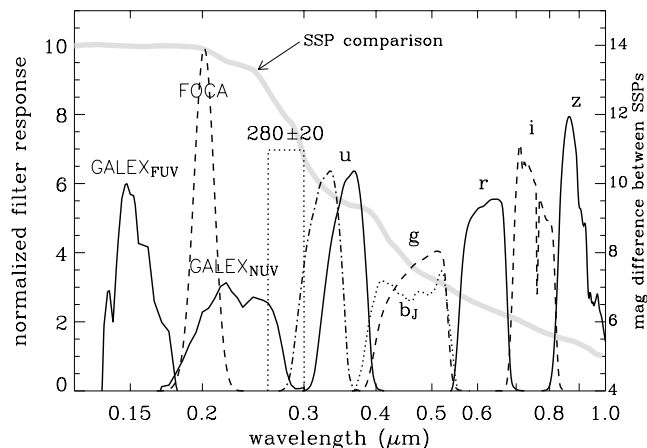
[*]E-mail: baldry@pha.jhu.edu

Figure 1. Filter profiles: *GALEX* (Martin et al. 2003); FOCA (Milliard et al. 1992); SDSS *ugriz* (Stoughton et al. 2002); APM b_J; and an artificial 280-nm band (Wolf et al. 2003). The *u* band shifted to $z = 0.1$ is shown by the dash-and-dotted line ($^{0.1}u$ band). Each curve is normalized so that the integral of the normalized transmission T d ln λ is equal to unity. Thus the height of each curve is related to its resolving power ($\lambda/\Delta\lambda$). The thick grey line represents the difference in magnitudes between dust-free 5- and 10 000-Myr simple stellar populations from the models of Bruzual & Charlot (2003) (the *y*-axis for this line is shown on the right).

luminosity is a reasonable measure of the SFR by comparing with other SFR indicators (Hα, O II and far-IR).

Fig. 1 shows the normalized responses of the *GALEX*, FOCA and SDSS filters. The difference between the spectra of a young and an old stellar population is also plotted. This shows (i) the importance of the *u* band in constraining the spectral energy distributions of galaxies between the *GALEX* UV bands and the visible bands, and (ii) the significantly increased sensitivity to young stellar populations of the *u* band in comparison with the *g* band.

While imaging data can be used to study correlations between properties of galaxies, in order to measure the space density of sources, it is preferable to select the targets for spectroscopic follow-up using the most appropriate band. The largest spectroscopic surveys at $z < 0.2$ are the SDSS (York et al. 2000), the 2dF Galaxy Redshift Survey (2dFGRS) (Colless et al. 2001) and the 6dF Galaxy Survey (6dFGS) (Jones et al. 2004), which have principally selected galaxies using the r, b_J and K bands, respectively ($\lambda_{eff} \approx 616$, 456 and 2160 nm). While the b_J selection is more biased toward star-forming galaxies than the other two, the band does not sample a majority of the light below the rest-frame 400-nm break at $z < 0.15$. In this paper, we describe the SDSS *u*-band Galaxy Survey (*u*GS), which provides an intermediate selection between the r/b_J and the *GALEX* bands, and a local sample for comparison with higher redshift surveys that are selected at similar rest-frame wavelengths [e.g. Deep Extragalactic Evolutionary Probe 2 (DEEP2), Davis et al. 2003]. The *u* band integrates flux almost entirely from below the 400-nm break ($\lambda_{eff} \approx 355$ nm).[1]

The plan of the paper is as follows: in Section 2 we describe the basics of the SDSS (which can be skipped for those familiar with the main survey); in Section 3 we introduce the Southern Survey;

in Section 4 we present the results for the LFs (with more details in Appendix A); in Sections 5 and 6 we discuss and conclude; and in Appendix B we outline sky-subtraction corrections for SDSS *u*-band magnitudes. Note that magnitudes used in this paper are corrected for Milky Way (MW) extinction unless otherwise noted.

2 THE SLOAN DIGITAL SKY SURVEY

The Sloan Digital Sky Survey is a project, with a dedicated 2.5-m telescope, designed to image 10^4 deg^2 and obtain spectra of 10^6 objects (York et al. 2000; Stoughton et al. 2002; Abazajian et al. 2003, 2004). The imaging covers five broadbands, *ugriz* with effective wavelengths of 355, 467, 616, 747 and 892 nm, using a mosaic charge-coupled device (CCD) camera (Gunn et al. 1998). Observations with a 0.5-m photometric telescope (Hogg et al. 2001) are used to calibrate the 2.5-m telescope images using a standard star system (Fukugita et al. 1996; Smith et al. 2002). Spectra are obtained using a 640-fibre fed spectrograph with a wavelength range of 380–920 nm and a resolution of $\lambda/\Delta\lambda \sim 1800$ (Uomoto et al. 1999).

The imaging data are astrometrically calibrated (Pier et al. 2003) and the images are reduced using a pipeline PHOTO that measures the observing conditions, and detects and measures objects. In particular, PHOTO produces various types of magnitude measurement including: (i) 'Petrosian magnitudes', the summed flux in an aperture that depends on the surface-brightness (SB) profile of the object, a modified version of the flux quantity defined by Petrosian (1976); (ii) 'model magnitudes', a fit to the flux using the best fit of a de Vaucouleurs (1959) and an exponential profile (Freeman 1970); (iii) 'point-spread function (PSF) magnitudes', a fit using the local PSF. The magnitudes are extinction-corrected using the MW dust maps of Schlegel, Finkbeiner & Davis (1998). Details of the imaging pipelines are given by Lupton et al. (2001) and Stoughton et al. (2002).

Once a sufficiently large area of sky has been imaged, the data are analysed using 'targeting' software routines that determine the objects to be observed spectroscopically. The targets that are part of the 'main program' include: galaxies with $r_{petro} < 17.8$ ('MAIN selection'; Strauss et al. 2002); quasars selected by various colour criteria with $i_{PSF} < 19.1$ or 20.2 ('quasi-stellar object (QSO) selection'; Richards et al. 2002); and luminous-red galaxies (LRG) selected by colour cuts with $r_{petro} < 19.2$ or 19.5 ('LRG selection'; Eisenstein et al. 2001). The targets from all the samples are assigned to plates, each with 640 fibres, using a tiling algorithm (Blanton et al. 2003d).

3 THE SOUTHERN SURVEY AND SAMPLE SELECTION

The main program of the SDSS is concentrated in the Northern Galactic Pole (NGP), with only three 'stripes' ($2°.5$ wide) in the Southern Galactic Pole (SGP).[2] During the times when it is not possible to observe the NGP, the 'Southern Survey' has been in operation. This has involved repeat imaging of the middle SGP

---

[1] The SDSS *u* band has a small amount of contamination from around 710 nm. This corresponds to about a 0.02-mag effect for mid-K stars and galaxies of similar colour (Abazajian et al. 2004). We have not corrected for this because most of the galaxies in our sample are significantly bluer.

[2] In the nomenclature of SDSS, a 'stripe' consists of a Northern and a Southern 'strip' because there are gaps between the detectors, which are aligned in six camera columns. The two strips are interleaved to produce a contiguously imaged stripe. A 'run' is a continuous drift-scan observation of a single strip. See Stoughton et al. (2002) for details on nomenclature including the flags used to select the objects.

Table 1. Number of objects and spectra for *u*-band selected samples.

Sample selection	No. of objects	No. spectroscopically observed by SDSS (broken down by program)[a]								2dF[b]
		(1) MAIN	(2) QSO	(3) *u* band	(4) Low *z*	(5) Low *z*	(6) High *z*	Other	Total	
$u < 20.0$ (incl. unresolved)[c]	321768	18829	15061	5606	2888	1027	139	8317	51867	79
$u < 20.5$ & $\Delta_{sg} > 0.05$[d]	74901	22141	6825	7400	6687	1846	637	303	45839	104
$u < 21.0$ & $\Delta_{sg} > 0.05$[e]	146488	23502	10089	7536	9997	2200	2084	584	55992	109

[a]Number observed by various Southern Survey programs described in Section 3.2 and the total number for all the programs; up to JD 24 53228. [b]Number of 2dFGRS redshifts not observed by SDSS. Only two 2dFGRS fields overlap with the Southern Survey. [c]Sample used to assess star–galaxy separation; see Fig. 3 for redshift versus Δ_{sg} (equation 1). [d]Sample used to compute the galaxy LFs (4); see Fig. 2 for the redshift histograms, Section 4 for colour–colour plots, and Fig. 6 for spectroscopic completeness as a function of colour. [e]Sample used to assess completeness to fainter magnitudes; see Fig. 5 for completeness as a function of magnitude.
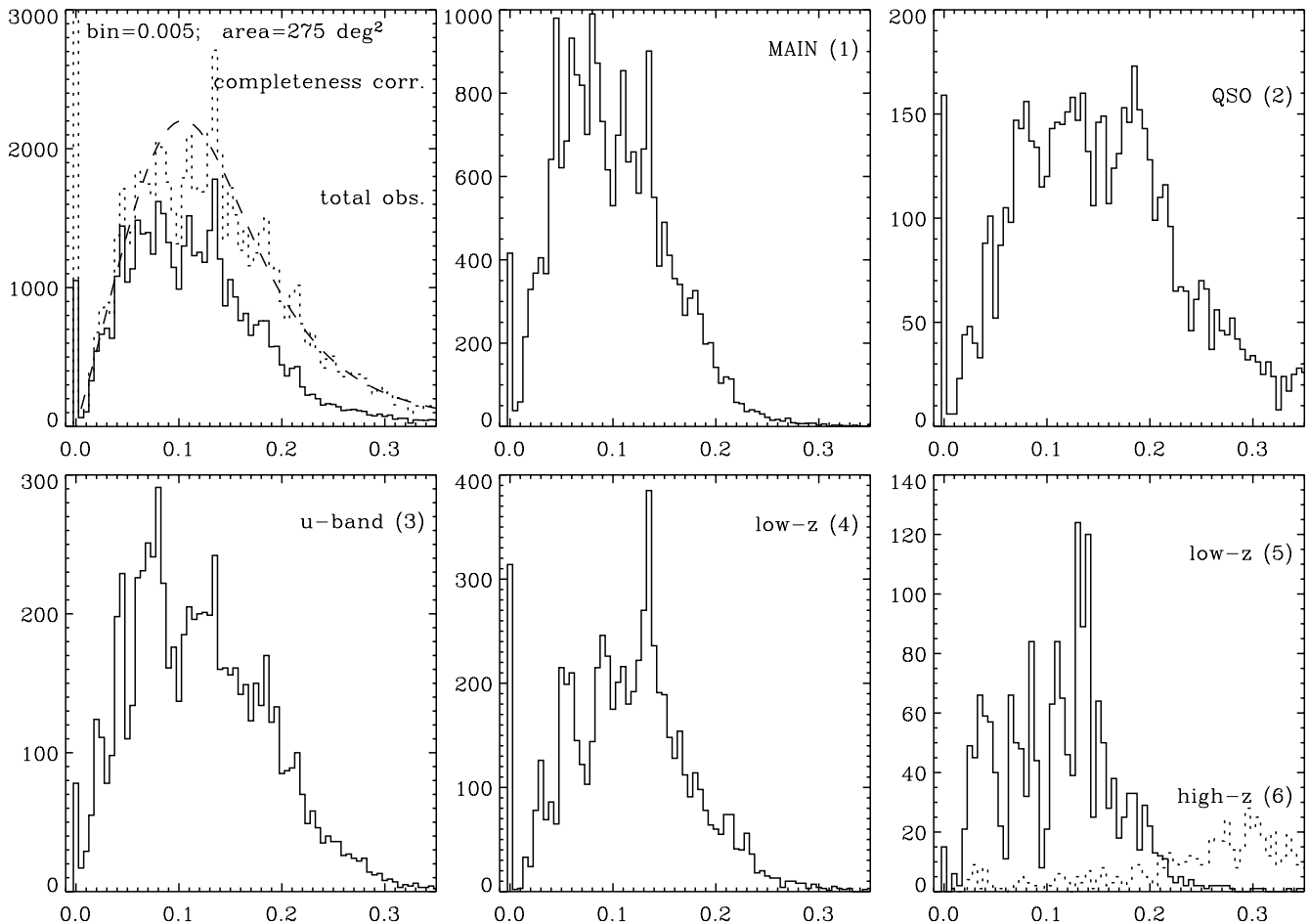

Figure 2. Redshift histograms ($u_{petro} < 20.5$ sample): number per 0.005 bin versus redshift. The top-left panel shows data from all the spectroscopic programs; with the solid line representing the observed data and the dotted line representing the completeness-corrected data (Section 3.3). The dashed line is a fit using equation (1) of Percival et al. (2001) with parameter values 0.158, 2.054 and 0.603. The other five panels show the data from the six programs described in Section 3.2. Note the *y*-axis scales vary; and the program names refer to the selection algorithms not the spectral classifications.

stripe (on the celestial equator) and additional non-standard spectroscopic observations. Here we define the Southern Survey region as RA from $-50\overset{\circ}{.}8$ to $58\overset{\circ}{.}6$ (20.6–3.9 h) and Dec. from $-1\overset{\circ}{.}26$ to $1\overset{\circ}{.}26$ (an area of 275.7 deg²). Over this region, there are 6–18 repeat images depending on the sky position with 253 unique spectroscopic plates observed (including 57 for the main program); up to JD 24 53228. The SDSS *u*GS consists of high signal-to-noise (S/N) ratio magnitude measurements using a co-added catalogue (Section 3.1), sky-subtraction corrections to *u*-band Petrosian magnitudes (Appendix B), and spectra selected in a variety of ways (Section 3.2) with completeness corrections for $u_{petro} < 20.5$ (Section 3.3).

These sections (Sections 3.1–3.3; Table 1; Figs 2–6) can be skipped or browsed for those not interested in the survey details at this stage.

3.1 Creating a co-added imaging catalogue

The repeat imaging data can be co-added at the image level or at the catalogue level. The former is necessary for increasing the depth of the imaging. Here we are mostly interested in improving the *u*-band Petrosian S/N ratio and associated colours. Therefore, it is adequate to co-add the data at the catalogue level because even the
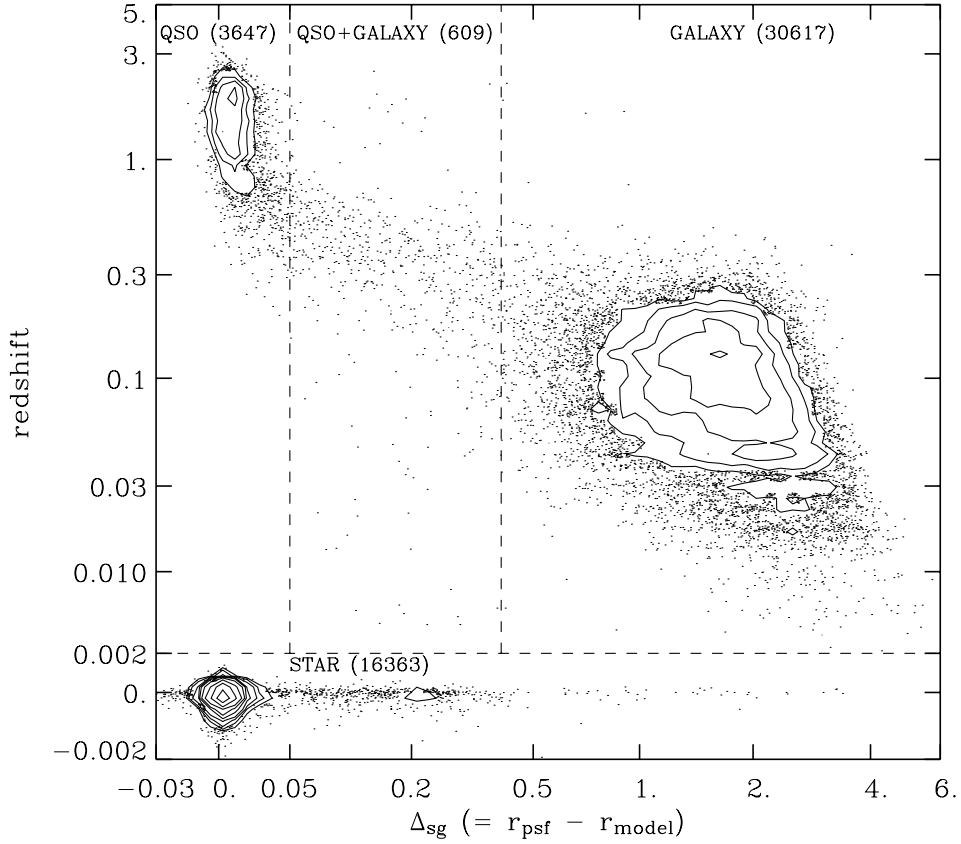
Figure 3. Redshift versus star–galaxy separation parameter for 51 236 objects with $u_{petro} < 20.0$. The dashed lines divide regions where the spectral classification is highly uniform (>99.9 per cent STAR; >99.9 per cent QSO; 99 per cent GALAXY) except for the QSO+GALAXY region, which has a mixed classification (77 and 23 per cent, respectively). The axes are linear in $\log(z + 0.004)$ and $\log(\Delta_{sg} + 0.1)$. The solid lines represent logarithmically spaced density contours with four contours per factor of 10. Note that there are no point sources ($\Delta_{sg} < 0.05$) with redshifts between 0.002 and 0.195. There are two one-dimensional spectral routines used for redshift and spectral classification within the SDSS collaboration (M. Subbarao et al. in preparation; D. Schlegel et al. in preparation). Only redshifts where the two routines produced similar results were included in this figure. This rejects only 1 per cent of the measured redshifts.
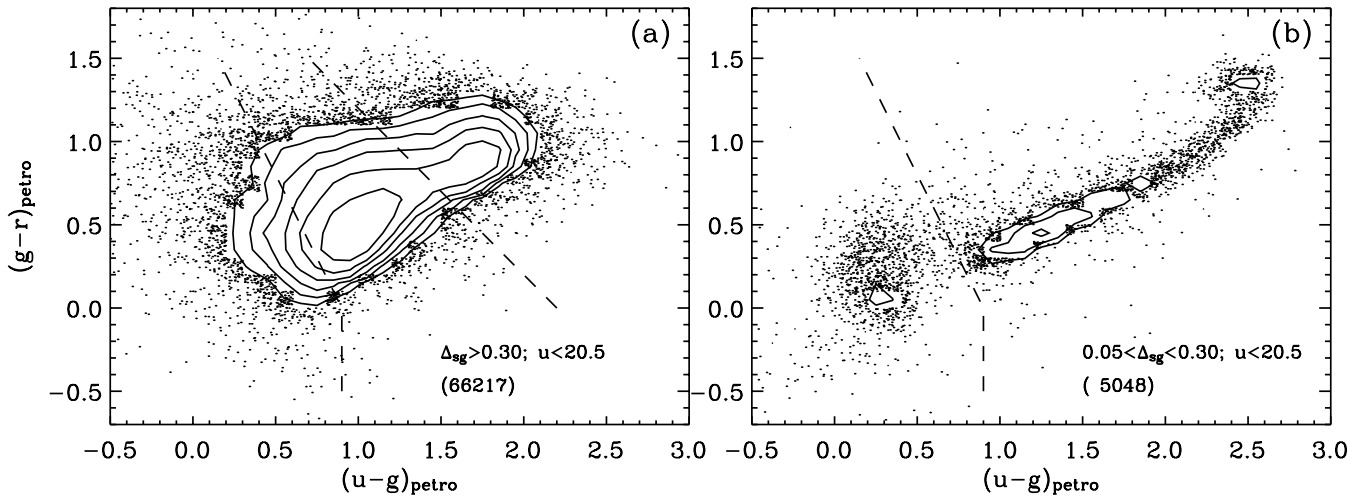

Figure 4. Observed colour–colour plots for (a) strongly resolved sources and (b) weakly resolved sources. The kinked dashed lines represent equations (7) and (8). Objects to the left of these could be selected by standard QSO selection (10 and 76 per cent of those observed are spectrally classified as QSO, for each panel, respectively). The straight dashed line [in (a)] represents an approximate division of the bimodality in the galaxy distribution ($u - r = 2.2$). Galaxies to the right are generally early types and those to the left are generally late types. The solid lines represent logarithmically spaced density contours with four contours per factor of 10. Note that, for this plot, objects were restricted to those with S/N > 5 in u, g and r, and with $u_{extinction} < 1$.
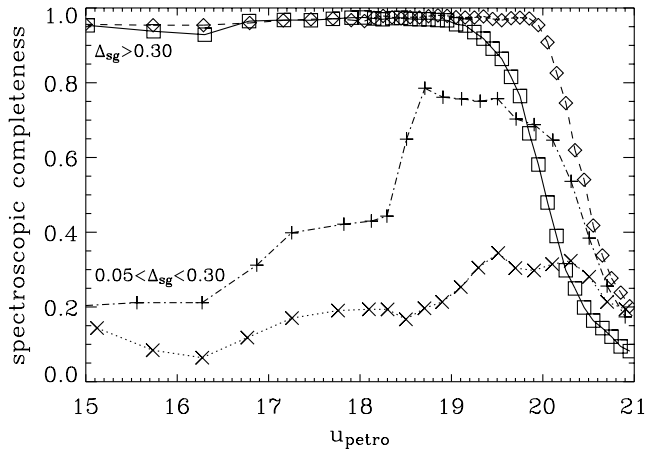
Figure 5. Average completeness versus *u*-band magnitude for different types of objects. The solid and dashed lines represent strongly resolved objects that are bluer and redder than $u - r = 2.2$, respectively (Fig. 4a); the dash-and-dotted and dotted lines represent weakly resolved objects that are bluer and redder than the approximate QSO cut, respectively [equations (7) and (8); Fig. 4b].

bluest galaxies in our sample are detected in the *g* and *r* bands with an adequate S/N ratio to define a Petrosian aperture. This has the advantage that the data passes through the standard imaging pipeline with no adjustments.

Our procedure for co-adding the catalogue was in two parts: (1) producing a master catalogue of groups of matched objects; and (2) selecting appropriate samples for analysis.

(1) First of all, each camera column and 'strip' is considered separately (see footnote 2). Catalogue objects are selected from all the runs so that they are: (i) unique to a run ('status_ok_run'); (ii) not near the edge of a frame (not 'object_edge') unless they are deblended from an edge object ('object_deblended_at_edge'); (iii) not 'bright', which refers to a preliminary identification of bright objects in the catalogue; (iv) not 'blended' unless they are the final product of a deblending process ('object_nodeblend' or 'nchild' = 0); and (v) detected in two or more of the the five bands, which is to remove cosmic rays and other artifacts only detected in one band. All the qualifying objects are then matched to objects in other runs within a radius of 1.5 arcsec. If there is more than one object from one run in a single matched group (which is rare but can occur because of deblending), then only the object that has the smallest deviation from the median r_petro value of the group is selected. Various mean and median values are calculated for the matched groups of objects, while the object flags are taken from the highest quality run. The SDSS asinh magnitudes (Lupton, Gunn & Szalay 1999) are converted to linear units before averaging (equation B2). This procedure produced a co-added catalogue of 6×10^6 objects.

(2) In addition to selecting on magnitudes, we apply the following criteria: (i) the object is detected in at least two bands out of *ugr* based on the best imaging run; (ii) the matched object is from a combination including over half of the maximum number of runs available at that sky position;[3] (iii) the object is not saturated in the fiducial *r* band; (iv) the S/N ratio of the Petrosian flux is greater than three in each of the *u*, *g* and *r* bands (the uncertainty is deter-

---

[3] Complex objects could have their centres shifted by more than the matching radius between runs and matching in more than half the runs ensures that only one copy of a complex object is included.

mined from the standard error over the co-added runs). The *u*-band Petrosian flux is adjusted for sky-subtraction errors (Appendix B) and if there are large differences between the median and mean *ugr* fluxes, the median is used to replace the mean value (and a modified standard error that excludes the minimum and maximum values is used). For the SDSS *u*GS, we selected resolved sources with $u_\mathrm{petro} < 20.5$.

The data from the co-added imaging catalogue that we use for the science results in this paper are: the mean Petrosian fluxes (median for $\sim$3 per cent of objects); the standard errors of the fluxes[4] (+2 per cent error added in quadrature for *k*-correction fitting); the median $r_\mathrm{PSF} - r_\mathrm{model}$ values (for star–galaxy separation); the mean sky positions; and the mean Petrosian half-light radii. The median S/N ratio of the co-added-catalogue Petrosian *u*-band fluxes at $u \sim 20.5$ is 10, which is a factor of $\sim$3 improvement over a single epoch of imaging.

3.2 Spectroscopic target selections

In addition to repeat imaging along the Southern Survey equatorial stripe, there are also extra spectroscopic observations. There are six general programs that contribute most of the redshifts to a $u_\mathrm{petro} < 20.5$ galaxy sample including specifically designed selection criteria for this survey.

For the selection, star–galaxy separation and SB parameters are defined as follows:

$$\Delta_\mathrm{sg} = r_\mathrm{PSF} - r_\mathrm{model} \tag{1}$$

$$\mu_{r,50} = r_\mathrm{petro} + 2.5 \log \left(2\pi R_{r,50}^2 \right), \tag{2}$$

where $R_{r,50}$ is the radius containing half the Petrosian flux. Thus $\mu_{r,50}$ is the mean SB within the Petrosian half-light radius. Note that most of the targets were selected using a single epoch of imaging before any co-added imaging catalogue was produced.

(1) *MAIN selection.* Many of the spectra were targeted as part of the main galaxy sample. This has the following basic criteria:

$$r_\mathrm{petro} < 17.8 \tag{3}$$

$$\mu_{r,50} < 24.5 \tag{4}$$

$$\Delta_\mathrm{sg} > 0.25. \tag{5}$$

See Strauss et al. (2002) for details. In addition to the main program, galaxy targets that were missed, because of fibre-placement restrictions or photometric errors, were included on additional plates. Thus the completeness of the MAIN selection is very high ($\approx$99 per cent) over much of the Southern Survey.

(2) *QSO selection.* SDSS quasars were selected by looking for non-stellar colours using PSF magnitudes. For the low-redshift candidates there was no requirement that the object be a point source. This enables selection of resolved galaxies where the central light may be dominated by a quasar but the total light may not be. The low-redshift (i.e. extended sources) selection in the main program can be approximated by

$$i_\mathrm{PSF} < 19.1 \tag{6}$$

---

[4] The standard error is $\sigma/\sqrt{N}$; while the modified error is given by $1.3\,\sigma_\mathrm{mod}/\sqrt{N-2}$ when using the median flux, where σ_mod is the standard deviation excluding the minimum and maximum values. The factor of 1.3 is determined from the median of $\sigma/\sigma_\mathrm{mod}$ for the data.
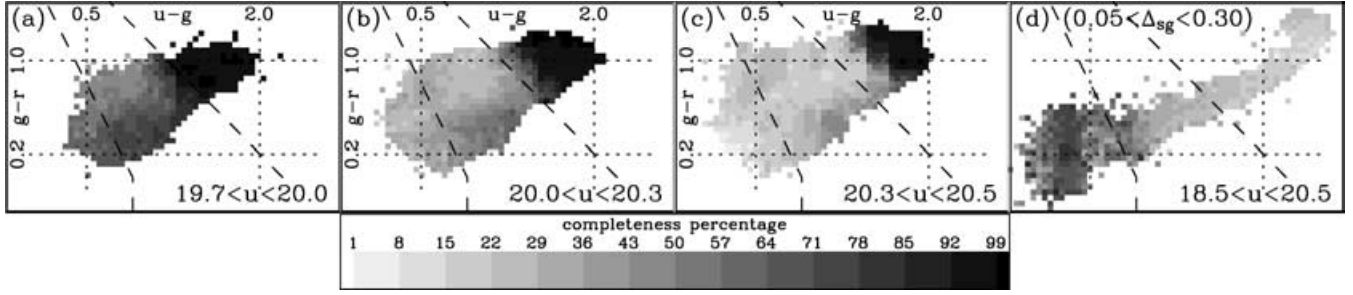
Figure 6. Completeness as a function of $g - r$ versus $u - g$ for (a–c) strongly resolved sources with various magnitude ranges and (d) weakly resolved sources. Note there are no areas with <1 per cent completeness so the white areas represent <5 objects per 0.05×0.05 colour bin [<2 objects in (d)] . The dashed lines represent the same colour cuts as in Fig. 4, which shows the number densities.

$$u_{\mathrm{PSF}} - g_{\mathrm{PSF}} < 0.9 \tag{7}$$

$$u_{\mathrm{PSF}} - 0.5 g_{\mathrm{PSF}} - 0.5 r_{\mathrm{PSF}} < 0.9. \tag{8}$$

See Richards et al. (2002) for details (e.g. fig. 13 of that paper). In addition to the main program, several alternative target selections were made on additional plates. These included probing closer to the stellar locus (and also closer to the galaxy locus), in the stellar locus (Vanden Berk et al. 2005) and selecting fainter QSO candidates.

(3) *u-band galaxy selection.* Here the idea was to was to obtain a complete *u*-band magnitude-limited galaxy sample by filling in the redshifts missed by other selections. The criteria were mostly as follows:

$$u_{\mathrm{select}} < 19.8 \tag{9}$$

$$g_{\mathrm{petro}} < 20.5 \tag{10}$$

$$r_{\mathrm{petro}} < 20.5 \tag{11}$$

$$\mu_{r,50} < 24.5 \tag{12}$$

$$\Delta_{\mathrm{sg}} > 0.2, \tag{13}$$

where $u_{\mathrm{select}} = u_{\mathrm{model}} - r_{\mathrm{model}} + r_{\mathrm{petro}}$, which can be regarded as a pseudo-Petrosian *u*-band magnitude. The reason for using this magnitude definition was to avoid u_{petro} (single epoch), which has larger Poisson noise and systematic errors (Appendix B), and has a greater susceptibility to imaging artifacts. The *g*- and *r*-band requirements were also used to reduce artifacts. On some plates, the magnitude criteria were relaxed by 0.2 mag to $u_{\mathrm{select}} < 20.0$.

(4) *Low-z galaxy selection.* Targets were selected using photometric redshifts with primarily

$$z_{\mathrm{photo}} < 0.15 \tag{14}$$

$$r_{\mathrm{petro}} < 19.0 \tag{15}$$

$$\Delta_{\mathrm{sg}} > 0.15. \tag{16}$$

The photometric technique was calibrated using spectroscopically confirmed redshifts from the main program and the Southern Survey. In order to test selection effects, other photometric redshift ranges were also sparsely sampled as were galaxies with $19.0 < r_{\mathrm{petro}} < 19.5$.

(5) *Low-z galaxy selection* (precursor). Targets were selected using photometric redshifts with primarily:

$$z_{\mathrm{photo}} < 0.2 \tag{17}$$

$$i_{\mathrm{petro}} < 20.0 \tag{18}$$

$$\Delta_{\mathrm{sg}} > 0.15. \tag{19}$$

These plates were also designed to be complimentary to the higher photometric redshift selection described below.

(6) *High-z galaxy selection.* Here the idea was to obtain spectroscopic redshifts for non-LRG galaxies above redshift 0.3 in order to improve photometric redshifts for these types of galaxies. The targets were selected with

$$z_{\mathrm{photo}} > 0.3 \tag{20}$$

$$r_{\mathrm{model}} < 19.5 \tag{21}$$

$$\Delta_{\mathrm{sg}} > 0.15. \tag{22}$$

In detail, the photometric redshift cut was converted to a series of colour and magnitude cuts.

Spectra were matched to photometric objects within 1.5 arcsec or within $R_{r,50}$ (1.5–12 arcsec, which accounts for 44 objects where an earlier version of PHOTO may have targeted a deblended piece of the galaxy). The number of spectra contributing to various *u*-band selected samples are shown in Table 1. Fig. 2 shows the redshift histograms. Other selections include stellar programs for unresolved sources and about 100 redshifts were included from the 2dFGRS (which is similar to $g \lesssim 19$ galaxy selection).

3.3 Completeness corrections

To determine spectroscopic completeness corrections, we do not attempt to back track and reproduce the above selection criteria. Many of the criteria are complicated and somewhat arbitrary for creating a *u*-band magnitude-limited sample. In addition, the photometric code and imaging run varies between selections and our aim is to select using Petrosian magnitudes from a co-added catalogue. Instead we use an empirical approach for estimating the completeness factors (C), which we define as the fraction of photometric objects that have been observed spectroscopically.

Before describing the completeness corrections, we discuss star (–quasar)–galaxy separation. For each object we used the median Δ_{sg} value ($= r_{\mathrm{PSF}} - r_{\mathrm{model}}$) from the co-added imaging for robustness. Fig. 3 shows redshift versus Δ_{sg} for a spectroscopic sample with $u_{\mathrm{petro}} < 20.0$ (Table 1). We define four regimes: sources with intragalactic redshifts ($z < 0.002$); and unresolved ($\Delta_{\mathrm{sg}} < 0.05$), weakly resolved ($0.05 < \Delta_{\mathrm{sg}} < 0.4$) and strongly resolved ($\Delta_{\mathrm{sg}} > 0.4$) sources with extragalactic redshifts ($z > 0.002$). The main point to note is that there are no unresolved extragalactic sources

with redshifts less than about 0.2 in this sample. While there are certainly selection effects against targeting this type of object, we note that about 7000 of the point sources with redshifts were targeted at random (as part of testing the QSO selection; Vanden Berk et al. 2005). There are some weakly resolved sources at low redshift. In this regime, some objects are spectrally classified as quasars[5] and some as galaxies.

To determine completeness corrections, we divide the sample into bins using four variables: Δ_{sg}, u, $u - g$, and $g - r$. These are related to the primary selection variables described in Section 3.2. First, galaxies are divided into two samples based on a cut in Δ_{sg} at 0.3 (near the limit for MAIN selection). Fig. 4 shows $u - g$ versus $g - r$ distributions for the strongly resolved and weakly resolved sources (now divided at 0.3). The kinked dashed lines show the limit for QSO selection of extended sources (Richards et al. 2002) while the straight dashed line shows a cut at $u - r = 2.2$, which approximately divides the bimodality in the galaxy distribution (Strateva et al. 2001). The point to note is that the completeness will vary with position in this diagram, because of cuts in r, g or associated colours. In addition, photometric redshift selection will also depend strongly on these colours because the 400-nm break moves through the g band over the redshift range 0.0–0.3.

After dividing the sample using Δ_{sg}, for $u > 19.7$, the strongly resolved objects are divided into 0.1-mag bins and the weakly resolved into 0.2-mag bins. At brighter magnitudes, wider bins are used. These magnitude bins are further divided in $u - g$ and $g - r$ with from 2×2 to 16×8 colour bins such that there are a minimum of 50 objects per final bin. Note that we have not included SB as a variable which would be necessary for studying bivariate distributions involving SB (e.g. Cross et al. 2001; Blanton et al. 2003c).

Fig. 5 shows the average completeness as function of magnitude for four groups divided by Δ_{sg} and by colour. The completeness is higher for the strongly resolved objects, with the redder objects having higher completeness because of MAIN selection. In the weakly resolved group, the bluer objects have higher completeness because of QSO selection. For the group dominated by late-type galaxies (solid line in Fig. 5), the average completeness is 88 per cent at $u = 19.5$ dropping smoothly to 18 per cent at $u = 20.5$. Above this limit, the completeness drops below 2 per cent for some bins ($\Delta_{sg} > 0.3$). Fig. 6 shows completeness as a function of colour.

For the SDSS uGS catalogue, we use the following selection criteria from the *co-added imaging catalogue* (Section 3.1)

$$u_{petro} < 20.5 \tag{23}$$

$$g_{petro} < 21.0 \tag{24}$$

$$\Delta_{sg} > 0.05 \tag{25}$$

$$u_{extinction} < 1.4. \tag{26}$$

The later cut on MW extinction only excludes objects over $\approx 0.7\,\text{deg}^2$ around a RA of $58.4°$.[6] We have not included an explicit SB limit because the production of the co-added catalogue (Section 3.1) is robust to low-SB artifacts. However, there is an implicit limit because of the pipeline reduction (Blanton et al. 2004). This does not

affect our results significantly, which are focused on the luminosity density (LD) measurements.

The catalogue includes 74 901 objects, of which, 45 839 have been observed spectroscopically with SDSS (see Table 1 for breakdown by program), and 104 with the 2dFGRS; the average completeness is 61 per cent. The limit has been extended to 20.5 rather than stopping at the 19.8/20.0 limit of the u-band selection (item (3) of Section 3.2) because pipeline flux changes and the other selections allow this. In other words, all galaxy spectral types are sufficiently sampled spectroscopically as faint as $u \approx 20.5$. Note that even at this limit, the redshift reliability is very high (≈ 99 per cent) because galaxies are either bright enough in the visible ($r_{petro} < 19$) or they very likely have strong emission lines. We assume that all the measured redshifts (D. Schlegel et al. pipeline) are correct for calculating the LFs.

4 GALAXY LUMINOSITY FUNCTIONS

From the uGS catalogue (equations 23–26), galaxies are selected with spectroscopic redshifts in the range $0.005 < z < 0.3$ and with magnitudes in the range $14.5 < u < 20.5$. In addition, we remove weakly resolved sources ($\Delta_{sg} < 0.3$) that are spectrally classified as a QSO (see footnote 5). In other words, only galaxies where the integrated visible flux is dominated by stellar light are included. These selections produce a sample of 43 223 galaxies. Note that compact non-QSO galaxies ($\Delta_{sg} < 0.3$) contribute <1 per cent to the LD.

Following Blanton et al. (2003b), we k correct to the rest-frame band equivalent to the observed u band at $z = 0.1$, which is called the $^{0.1}u$ band ($\lambda_{eff} \approx 322$ nm; FWHM ≈ 53 nm). The absolute magnitude on the AB system (Oke & Gunn 1983) is given by

$$M_{322} = u_{petro} - k_{0.1u,u} - 5\log(D_L/10\,\text{pc}) - 0.04 \tag{27}$$

where D_L is the luminosity distance for a cosmology with (Ω_m, Ω_Λ)$_0$ = (0.3,0.7) and $H_0 = (h_{70})\,70\,\text{km s}^{-1}\,\text{Mpc}^{-1}$ and $k_{0.1u,u}$ is the k correction using the method of Blanton et al. (2003a) (see, e.g. Hogg et al. 2002 for a general definition of the k correction). The -0.04 term is the estimated correction from the SDSS u-band system to an AB system (Abazajian et al. 2004).[7]

To calculate the galaxy LFs, we divide the sample into 0.02-redshift slices and 0.2-mag bins. For each bin, the LF is then given by

$$\phi_M\,dM = \sum_i \frac{1}{C_i\,V_{max,i}}, \tag{28}$$

where C is the spectroscopic completeness (Section 3.3), and V_{max} is the comoving volume over which the galaxy could be observed (Schmidt 1968) *within* the redshift slice and within the magnitude limits of $14.5 < u < 20.5$. Each redshift slice is cut in absolute magnitude so that the sample is nearly volume limited ($0.9 < V_{max}/V_{slice} \leqslant 1$ for $\sim$95 per cent of the galaxies). The volumes of each slice range from 2×10^4 Mpc^3 ($z = 0.005$–0.02) to 8×10^6 Mpc^3 ($z = 0.28$–0.30).

Fig. 7(a) shows the binned galaxy LFs for the 15 redshift slices out to $z = 0.3$. The dominant effect is that the function shifts toward higher luminosities with increasing redshift.

---

[5] By spectral classification as a QSO, we mean a spectrum with broad emission lines, i.e. classified as a type 1 (unobscured) AGN. There is no consideration of luminosity or (narrow-)line ratios.

[6] The area lost to bright stars is also small (<1 deg^2 in total), e.g., around the $V = 3$ star HR8414 and the globular cluster M2. We assume the area of the survey is 275 deg^2 for calculating galaxy number and luminosity densities.
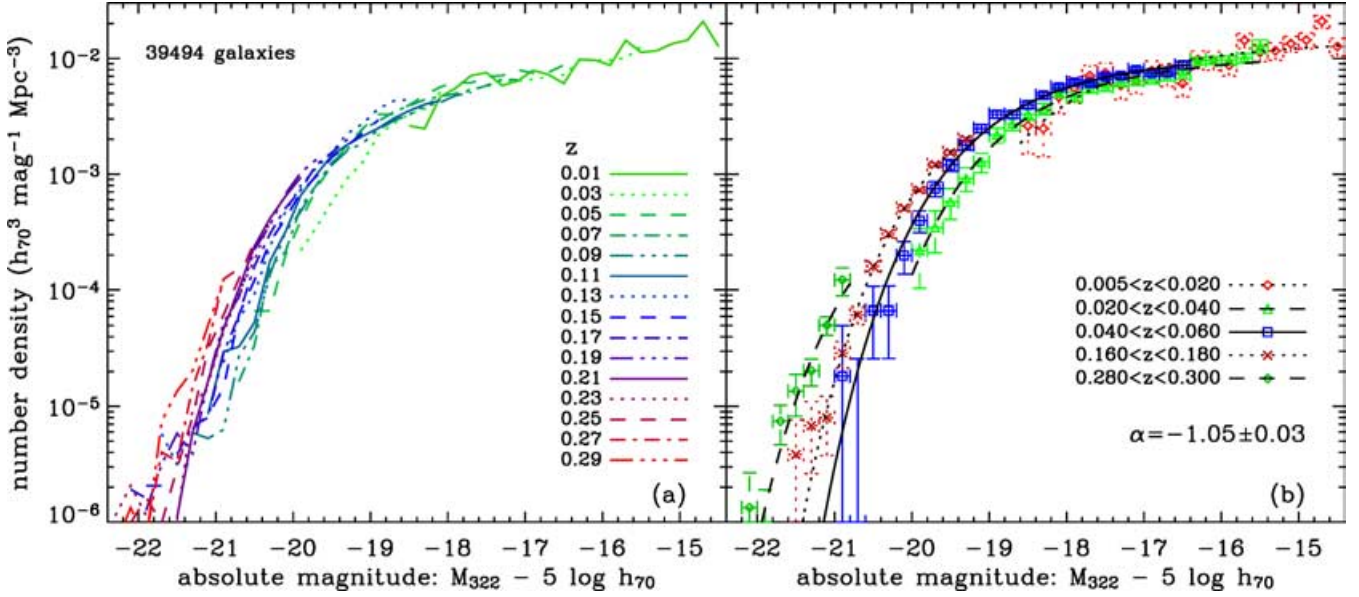
[7] The SDSS photometry was originally designed to be calibrated to an AB scale but because of filter variations between the natural system of the telescope and the standard star system it has been modified (Abazajian et al. 2003).

Figure 7. Near-UV $^{0.1}u$ LFs for galaxies with $0.005 < z < 0.3$. The lines represent different redshift slices. The binning is 0.02 in redshift and 0.2 in magnitude. There is a clear increase in the comoving density of luminous galaxies with increasing redshift. Panel (a) shows the binned functions, while panel (b) shows the binned-function error bars and Schechter fits for the three lowest redshift slices and two others (fixed α). The full sample over the redshift range includes 43 223 galaxies, which is reduced to 39 494 by making the slices nearly volume limited.

The general form of the LFs can be parameterized using the Schechter (1976) function, which is given by

$$\phi_L \, dL = \phi^* \left(\frac{L}{L^*} \right)^\alpha e^{-L/L^*} \frac{dL}{L^*} \tag{29}$$

where $\phi_L \, dL$ is the comoving number density of galaxies with luminosity between L and $L + dL$, L^* is the 'characteristic luminosity' (for the exponential cut-off), ϕ^* is the 'characteristic number density' and α is the 'faint-end slope'. This equation is converted to magnitude form, with M^* as the 'characteristic magnitude', and the slope is then $-0.4(\alpha + 1)$ in a log number density versus magnitude plot. We use this parametric form to quantify the evolution in terms of M^* and ϕ^*.

Before quantifying the evolution, we determine the faint-end slope. The density of galaxies fainter than -17 is only determined for the three lowest redshift slices. On the assumption that the faint-end slope does not vary, we fit the best-fitting slope over these lowest slices ($z < 0.06$). The Schechter fits are shown in Fig. 7(b). The best-fitting faint-end slope is given by

$$\alpha = -1.05 \pm 0.03 \, [\pm 0.07] \tag{30}$$

where the first uncertainty is the standard error from the Poisson noise, and the second uncertainty is an estimate of the systematic error, obtained by comparing with the best fits using combinations of three out of the four lowest redshift slices (Fig. A1). These variations may reflect the fact that the Schechter function is not a perfect match to the LFs (and therefore depends on the magnitude range of the fitting), there may be systematic uncertainties because of photometric deblending or astrophysical changes because of large-scale structure.

Assuming that the faint-end slope does not vary significantly with redshift, we can then characterize with more precision the evolution of the exponential cut-off shown clearly in Fig. 7. To do this, we restrict the fitting to α between -1.15 and -0.95. For each redshift slice, M^* and ϕ^* are fitted marginalizing over the allowed range of α (Table A1). For the four highest redshift slices ($z > 0.22$), $\log \phi^*$ is

constrained to be greater than -2.2; and for the lowest redshift ($z < 0.02$), M^* is constrained to be brighter than -18.4. This is because these parameters are not realistically fitted in these regimes.

Fig. 8 shows the evolution in the Schechter parameters. There is a highly significant detection of evolution in M^* with a slope of -3.1 ± 0.2 per redshift. This means that the exponential cut-off becomes more luminous by about 0.9 mag between redshifts 0.0 and 0.3. There is a marginal detection of evolution in ϕ^*, which is more strongly affected by cosmic variance. This is only a 1.5σ detection using the redshift slices up to 0.22. The fits to the evolution are given in Table 2. Note that the results (for M^* in particular) depend significantly on assumptions about α, for example, for $\alpha = -1.05$ strictly fixed we obtain an M^* evolution slope of -2.5 ± 0.1. Thus, M^* gets more luminous by 0.8 ± 0.1 mag ($z = 0.0$–0.3) depending on the details of the LF evolution.

The lowest redshift slice was not included in the M^* evolution fit. This was to avoid problems with measuring bright nearby galaxies using the SDSS pipelines. Large galaxies may be too strongly deblended (SB fluctuations are more significant at low redshift), or the Petrosian aperture may not be large enough. In these cases, the flux of the galaxies will be underestimated.

The Schechter function allows for an estimate of the total comoving LD assuming that the function remains valid outside the magnitude range of the fitting. This LD is given in magnitudes per cubic megaparsec by

$$j = M^* - 2.5 \log \left[(\phi^*/\text{Mpc}^{-3}) \, \Gamma_f(\alpha + 2) \right], \tag{31}$$

where Γ_f is the gamma function; and in linear units by

$$\rho_L = 10^{(34.1 - j)/2.5} \; \text{W Hz}^{-1} \, \text{Mpc}^{-3} \tag{32}$$

from j in AB mag Mpc^{-3}. If we assume that ϕ^* and α are constant then the evolution in M^* also represents the evolution in the comoving LD. However, we cannot rule out contributions from variations in ϕ^* (or α) to the evolution. Fig. 9 shows the evolution in the LD
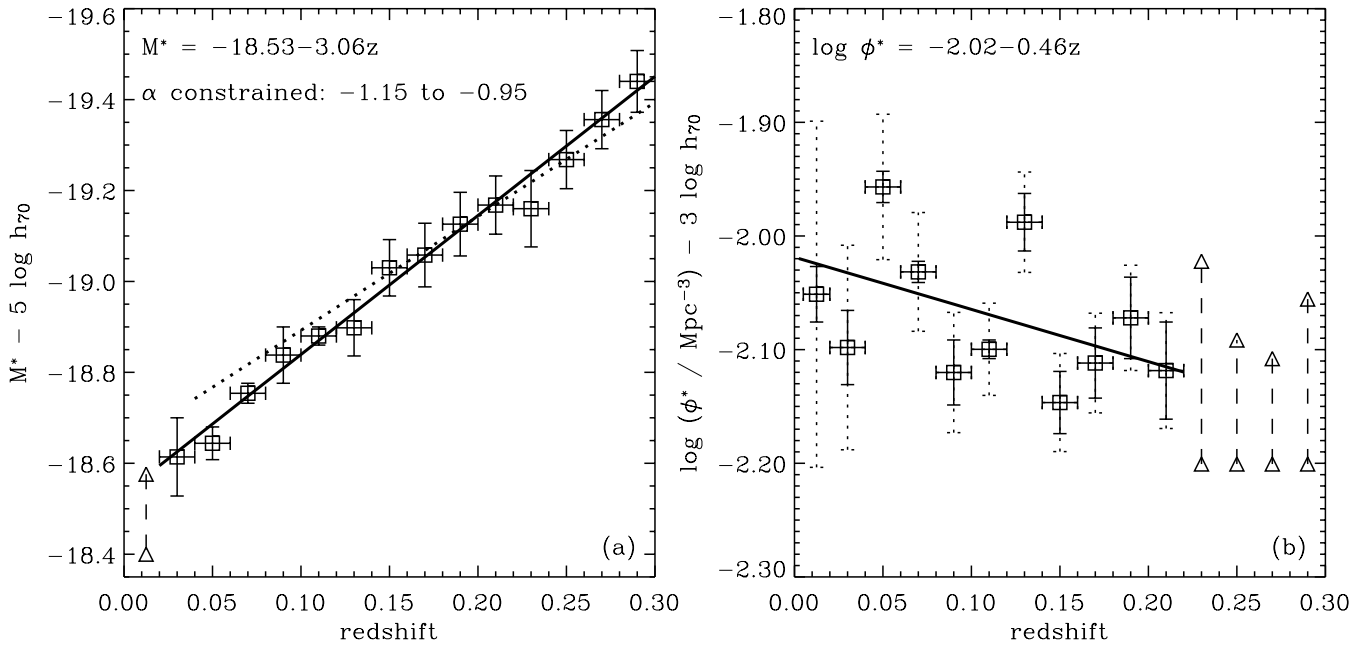
Figure 8. Evolution in the $^{0.1}u$ LFs characterized by the Schechter parameters M^* and ϕ^*. The faint-end slope α is assumed to be in the range -1.15 to -0.95. The squares with solid error bars represent standard errors while the dotted error bars [in (b)] represent standard errors plus an error added in quadrature to account for cosmic variance (Appendix A). The triangles with dashed lines represent the 1σ ranges when the fitting if restricted to $M^* < -18.4$ or $\log \phi^* > -2.2$. The thick solid lines represent fits to the evolution over the range shown (Table 2). The dotted line [in (a)] represents a fit with fixed $\alpha = -1.05$.

Table 2. Straight line fits to evolution in the Schechter parameters and the LD.

Parameter (322-nm band)	Redshift fitting range	Line intercepts ($z = 0.0$)	($z = 0.1$)	($z = 0.2$)	Line slope (per unit z)	β value[a]
$M^* - 5\log h_{70}$ (mag)[b]	0.02–0.30	-18.53 ± 0.02	-18.84 ± 0.01	-19.15 ± 0.02	-3.06 ± 0.18	3.3 ± 0.2
$\log(\phi^*/\mathrm{Mpc}^{-3}) - 3\log h_{70}$	0.00–0.22	-2.02 ± 0.04	-2.06 ± 0.02	-2.11 ± 0.03	-0.46 ± 0.31	-1.2 ± 0.8
$j + 2.5\log h_{70}$ (mag Mpc^{-3})	0.00–0.30	-13.47 ± 0.07	-13.68 ± 0.03	-13.89 ± 0.06	-2.12 ± 0.55	2.2 ± 0.6
$M^* - 5\log h_{70}$ (mag)[c]	0.04–0.30	-18.64 ± 0.02	-18.89 ± 0.01	-19.14 ± 0.01	-2.51 ± 0.12	2.7 ± 0.1
$\log(\phi^*/\mathrm{Mpc}^{-3}) - 3\log h_{70}$	0.00–0.22	-2.05 ± 0.04	-2.08 ± 0.02	-2.11 ± 0.02	-0.27 ± 0.29	-0.7 ± 0.8
$j + 2.5\log h_{70}$ (mag Mpc^{-3})	0.00–0.30	-13.53 ± 0.06	-13.71 ± 0.03	-13.89 ± 0.03	-1.80 ± 0.37	1.9 ± 0.4

[a]Fit to linear measurements (L^*, ϕ^* and ρ_L), with a function $\propto (1+z)^\beta$. [b]For the first set of fits, the results were marginalized over the faint-end slope: α in the range -1.15 to -0.95. By comparison with fixed α results, estimates of the systematic uncertainties are 0.05 in M^*, 0.02 in $\log \phi^*$ and 0.04 in j for the intercepts. [c]For the second set of fits, the faint-end slope was fixed: $\alpha = -1.05$. Note here the 0.02–0.04 slice is an outlier in M^* (Table A1), which may reflect photometric errors or large-scale structure variations.

that includes the variation in ϕ^*. Parameterizing the evolution as

$$\rho_L \propto (1+z)^\beta \qquad (33)$$

as per, for example, Lilly et al. (1996), then we obtain $\beta = 2.2 \pm 0.6$ for the 322-nm LD. In Section 5.2, we combine these measurements with COMBO-17 at $0.2 < z < 1.2$ (Wolf et al. 2003).

5 DISCUSSION

5.1 Comparison with $z \sim 0.1$ luminosity functions

The first test we make is to compare with the SDSS results of Blanton et al. (2003b) that used the same band. For the $^{0.1}u$ LF, their sample included 22 020 galaxies with $u < 18.4$ in the redshift range $0.02 < z < 0.14$. The u limit was chosen in order to avoid significant bias from the $r < 17.8$ MAIN selection, i.e. because 99 per cent of galaxies have $u - r \gtrsim 0.6$ [Fig. 4(a)]. The fitting used a maximum

likelihood method, with a general shape for the LF, that incorporated luminosity and number evolution. The results obtained (by fitting a Schechter function) were $M^* = -18.70 \pm 0.03$, $\alpha = -0.92 \pm 0.07$ and $j = -13.71 \pm 0.14$ at $z = 0.1$ (after converting to $H_0 = 70$). The faint-end slope and LD are in 2σ statistical agreement with our results while M^* is not (0.14 mag difference). However, if we set α to be -0.92 in our analysis, the discrepancy is reduced. In addition, we used fixed 0.2-mag bins whereas they used multiple-Gaussian fitting. Note also that there are less than 4000 galaxies in common between the two data sets (<20 per cent of theirs and <10 per cent of ours).

Parameters were used to include evolution in the luminosity and number density (Lin et al. 1999). In terms of the evolution fitting given in Table 2, the results of Blanton et al. can be considered as -4.2 ± 0.9 for M^* and $+1.3 \pm 1.3$ for $\log \phi^*$ (both per unit z). These evolution parameters are in agreement with our results within 2σ.

Using the uGS, we have improved on the accuracy of the $^{0.1}u$ LF and evolution compared to using the main galaxy sample selected in the r band (which was of course a strong motivation for this survey).
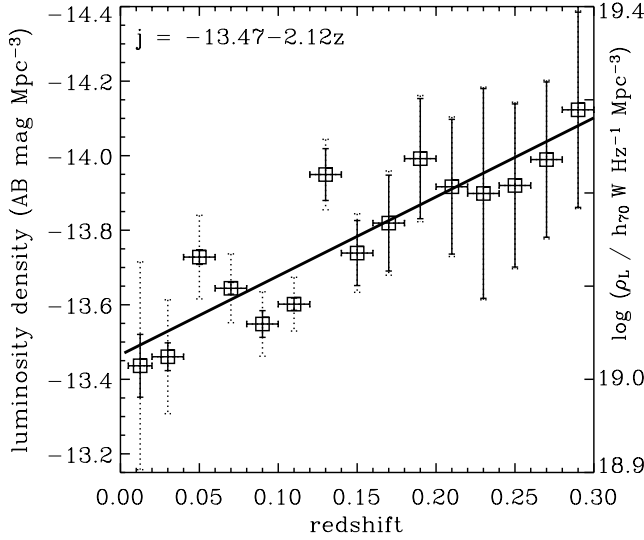
Figure 9. Evolution in the $^{0.1}u$ comoving LD. See Fig. 8 for symbols and details of the line styles.
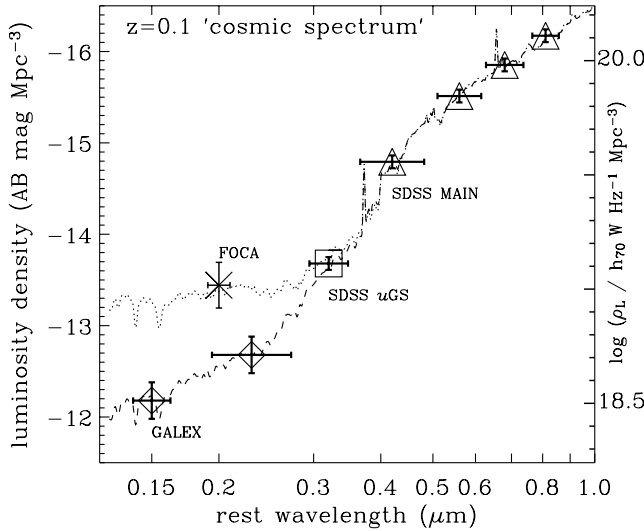

Figure 10. Luminosity densities at $z = 0.1$ from SDSS, FOCA and *GALEX*. The square represents the $^{0.1}u$ result of this paper; the triangles, the $^{0.1}griz$ results of Blanton et al. (2003b); the cross, the FOCA result of Sullivan et al. (2000); and the diamonds, the *GALEX* results of Budavári et al. (2005). The horizontal bars represent the *FWHM* of each band. The best-fitting Fioc & Rocca-Volmerange (1997, 1999) population-synthesis model from the fitting of Baldry & Glazebrook (2003) is shown by the dotted line; and a new best-fitting model that uses the *GALEX* results is shown by the dashed line.

For example, the $^{0.1}u$ LD is now known to comparable accuracy as the $^{0.1}griz$ bands measured by Blanton et al. (2003b). Fig. 10 shows the $z = 0.1$ luminosity densities from the SDSS. The uncertainties are of order 5–10 per cent because of absolute calibration, SB selection effects, conversions to total galaxy magnitudes and estimates of the effective survey areas.

Fig. 10 also shows the luminosity densities from the balloon-borne FOCA telescope (Sullivan et al. 2000) and from the *GALEX* space telescope (Budavári et al. 2005). The former was derived from $2.2 \deg^2$ over $0.0 < z < 0.4$ and the latter from $44 \deg^2$ over $0.07 < z < 0.13$. The earlier result is significantly higher in LD.

Also, Sullivan et al. obtained a faint-end slope of -1.5 ± 0.1, which is not in agreement with our measurements, while Budavári et al. obtained -1.1 ± 0.1, which is in good agreement. In Fig. 10, we also show two spectral models for the UV to near-IR 'cosmic spectrum' from the fitting of Baldry & Glazebrook (2003) (using PEGASE models; Fioc & Rocca-Volmerange 1997, 1999). We use the new fit to the *GALEX* plus SDSS measurements to obtain a correction from the $^{0.1}u$ band to a 280 ± 20 nm band (Fig. 1), which we use to compare with higher redshift measurements of rest-frame UV densities. This is given by

$$j_{280} \approx j_{322} + 0.45. \tag{34}$$

A similar correction is determined if we use the k-correction templates from Blanton et al. (2003a), i.e. k correcting to the $\sim {}^{0.3}u$ band, but this is less reliable because the $z \sim 0.1$ LF then requires significant wavelength extrapolation from the observed bands.

Our low-redshift ^{0}u results (Table A1) are also in good agreement with those determined in nearby clusters by Christlein, McIntosh & Zabludoff (2004). They found $M_U^* = -18.9 \pm 0.3$ (converting to AB mag) and $\alpha_U = -1.1 \pm 0.2$.

5.2 Evolution in comoving luminosity densities

In order to compare with redshifts out to $z \sim 1$, we take near-UV LD measurements from the literature (Lilly et al. 1996; Connolly et al. 1997; Wilson et al. 2002; Wolf et al. 2003; Budavári et al. 2005; Wyder et al. 2005) and convert them to the $(\Omega_m, \Omega_\Lambda)_0 = (0.3, 0.7)$ cosmology. This was done by making a comoving volume correction over the redshift range of each measurement and a luminosity correction for the midpoint redshift. Fig. 11 shows these measurements and our results converted to 280 nm, which show an increase in the LD with redshift. Our results and the results of COMBO-17 (both shown using solid-line error bars) cover a significantly larger volume than the other results (excepting the *GALEX* results). We fit to these SDSS and COMBO-17 results, and obtain

$$\beta_{280} = 2.07 \pm 0.14 \,[\pm 0.10], \tag{35}$$

where the first uncertainty is the standard error and the second is per 0.05 mag uncertainty in the equation (34) conversion. This represents the most accurate measurement of near-UV LD evolution to date and it rules out the steep evolution found by Lilly et al. (1996) and is closer to the gradual rates determined by Cowie et al. (1999) and Wilson et al. (2002). The equation (33) fit is shown by a solid line in Fig. 11(b), while a fit using $\rho_L \propto \exp(t/\tau)$, where t is the look-back time for our assumed cosmology, is shown by a dashed line. The exponential time-scale is given by $\tau_{280} = 5.5 \pm 0.4$ $[\pm 0.3]$ Gyr.

In the absence of dust and chemical evolution, the 280-nm density evolution corresponds closely to the SFR density. From a solar-metallicity population synthesis model (with a $\beta \sim 2$ star formation history): $\beta_{SFR} \sim \beta_{280} + 0.1$ and $\tau_{SFR} \sim \tau_{280} - 0.2$ Gyr. In other words, the evolution in the SFR is slightly steeper than that of the near-UV LD because of relatively small contributions from evolved stellar populations. Our results are consistent with that found using the far-UV by Schiminovich et al. (2005): $\beta_{150} = 2.5 \pm 0.7$.

Many other SFR indicators have been used to trace the cosmic star formation history, some of which are less sensitive to dust or can be corrected for dust. From a compilation of UV, [O II], $H\alpha$, $H\beta$, mid-IR, submillimetre radio and X-ray measurements, Hopkins (2004) found that $\beta_{SFR} = 3.3 \pm 0.3$ for $z < 1$ data when including SFR-dependent dust attenuation corrections where necessary. This is inconsistent with our result $\beta_{SFR} = 2.2 \pm 0.2$ that
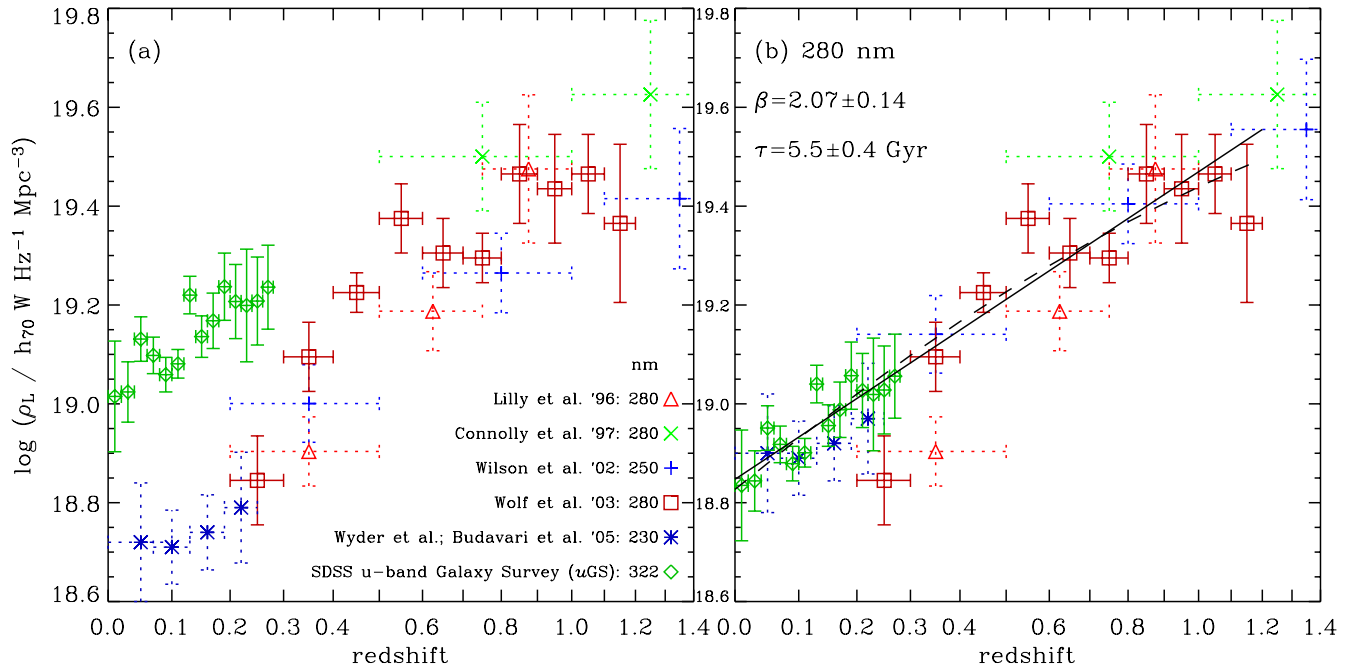
Figure 11. Evolution in the near-UV comoving luminosity densities. Various data measurements are shown by the symbols. Panel (a) shows the data at wavelengths 230, 250, 280 and 322 nm; while panel (b) shows the data adjusted to 280 nm where necessary. The corrections in $\log \rho_L$ were assumed to be -0.18, $+0.18$ and $+0.14$ for the $^{0.1}u$, *GALEX* NUV and Wilson et al. results, respectively (from the dashed-line fit in Fig. 10). Thus, the agreement between the results from this paper and from *GALEX* in (b) is by construction. The best fit to the data from this paper and from COMBO-17 (fig. 19 of Wolf et al.) is shown by a solid line using the parametrization of equation (33), and by a dashed line using an exponentially increasing LD with look-back time. The *x*-axis is linear in $\log(1 + z)$.

assumes no dust evolution. The results can be reconciled if the effective average attenuation at 280 nm increases by 0.8 ± 0.3 mag between $z = 0$ and 1. This is a plausible increase because the characteristic luminosities of rapidly star-forming galaxies are increasing with redshift (Cowie et al. 1996); and more luminous galaxies have higher levels of dust attenuation (Hopkins et al. 2001). However, we caution that our measured dust increase is not independent of that idea because of the SFR-dependent corrections used by Hopkins. Bolometric OB-star luminosity densities derived from far/near-UV and mid/far-IR wavelengths (with corrections for AGN and evolved stellar populations) could be used for an unambiguous measure of β_{SFR}.

5.3 Evolution in luminosity functions

While it is robust to compare our LD results with those of COMBO-17 using a model cosmic-spectrum correction, it is not so straightforward for assessing LF evolution. Any colour–magnitude relations and dispersion will affect the number density and shape of the LFs. Instead, the COMBO-17 data could be analysed to measure the LFs in the $^{0.1}u$ or the more standard ^0u band (Appendix A). Other large surveys for which our results could be compared are the VIMOS-VLT Deep Survey (VVDS; Le Fèvre et al. 2004) or the DEEP2 survey (Davis et al. 2003).

Comparing our ^0u results with the VVDS results of Ilbert et al. (2004), we find M^* brightens by 1.5–2 mag between $z = 0$ and 1. Fig. 12 shows the evolution in M^* versus redshift. To obtain the upper and lower limits, we fit to the SDSS data ($\pm 2\sigma$) and the VVDS data ($\pm 1\sigma$) allowing for the errors to all be in the same direction. There is a suggestion that M^* brightens more rapidly below $z = 0.5$ than above but the data are also consistent with a constant slope.
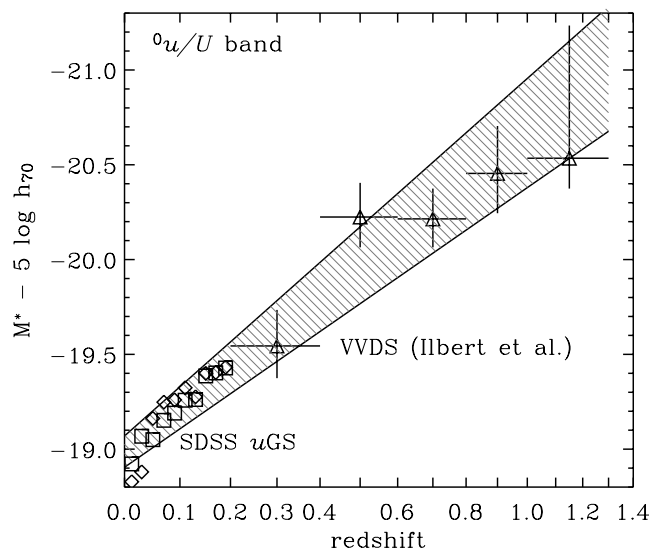

Figure 12. Evolution in M^* for the ^0u LFs. The squares and diamonds represent the results from this paper, marginalized over $\alpha = -1.15 \pm 0.10$ and fixed $\alpha = -1.15$, respectively (with errors approximately the size of symbols). The triangles represent the results from Ilbert et al. (2004) with α allowed to vary except for the highest redshift slice. The sloped-line region shows the range between the lower and upper straight line fits.

6 CONCLUSIONS

We have analysed a *u*-band selected galaxy survey, using spectroscopic completeness corrections as a function of colour and magnitude to account for inhomogeneous selection (Figs 2, 5 and 6). The main results are as follows.

(1) Testing star–galaxy separation (Fig. 3), we find that compact galaxies that could be missed by MAIN selection contribute insignificantly to the stellar UV LD (<1 per cent).

(2) The faint-end slope of the low-redshift $^{0.1}u$ LF is near flat: $\alpha = -1.05 \pm 0.08$. This was obtained from the best fit over the three lowest redshift slices ($z < 0.06$) with magnitudes from -21.4 to -14.4 [Fig. 7(b)].

(3) The evolution in the LFs is dominated by a luminosity shift (Figs 7 and 8), which can be characterized by a shift in M^* of -0.8 ± 0.1 mag between $z = 0$ and 0.3.

(4) In order to compare the UV LD evolution with COMBO-17 at higher redshifts (Wolf et al. 2003), we fit to LD measurements at $z = 0.1$ (Fig. 10) including recent *GALEX* results of Budavári et al. (2005), and obtain a correction to 280 nm of $+0.45$ mag. Our LD measurements versus redshift then lineup remarkably well with those of COMBO-17 (Fig. 11) and we find that the evolution can be parameterized by equation (33) with $\beta_{280} = 2.1 \pm 0.2$. This is a significantly shallower evolution than that found using other SFR indicators and is consistent with an increase in average dust attenuation of 0.8 ± 0.3 mag between $z = 0$ and 1.

Future work with the *u*GS could include: assessing the UV LF evolution for different classes of objects (e.g. AGN, late/early-type galaxies); measuring the Hα LF (modulo aperture and dust corrections); and studying multivariate distributions in a star-forming sample. These will enable a quantification of contributions to the near-UV decline at $z \lesssim 0.2$ from different galaxy populations and from dust and star formation.

ACKNOWLEDGMENTS

REFERENCES

Abazajian K. et al., 2003, AJ, 126, 2081
Abazajian K. et al., 2004, AJ, 128, 502
Baldry I. K., Glazebrook K., 2003, ApJ, 593, 258
Blanton M. R. et al., 2003a, AJ, 125, 2348
Blanton M. R. et al., 2003b, ApJ, 592, 819
Blanton M. R. et al., 2003c, ApJ, 594, 186
Blanton M. R., Lin H., Lupton R. H., Maley F. M., Young N., Zehavi I., Loveday J., 2003d, AJ, 125, 2276
Blanton M. R., Lupton R. H., Schlegel D. J., Strauss M. A., Brinkmann J., Fukugita M., Loveday J., 2004, ApJ, submitted (astro-ph/0410164)
Bruzual G., Charlot S., 2003, MNRAS, 344, 1000
Budavári T. et al., 2005, ApJ, 619, L31
Christlein D., McIntosh D. H., Zabludoff A. I., 2004, ApJ, 611, 795
Colless M. et al., 2001, MNRAS, 328, 1039
Connolly A. J., Szalay A. S., Dickinson M., Subbarao M. U., Brunner R. J., 1997, ApJ, 486, L11
Cowie L. L., Songaila A., Hu E. M., Cohen J. G., 1996, AJ, 112, 839
Cowie L. L., Songaila A., Barger A. J., 1999, AJ, 118, 603
Cross N. et al., 2001, MNRAS, 324, 825
Davis M. et al., 2003, Proc. SPIE, 4834, 161
de Vaucouleurs G., 1959, Handbuch Phys., 53, 311
Eisenstein D. J. et al., 2001, AJ, 122, 2267
Fioc M., Rocca-Volmerange B., 1997, A&A, 326, 950
Fioc M., Rocca-Volmerange B., 1999, preprint (astro-ph/9912179)
Freeman K. C., 1970, ApJ, 160, 811
Fukugita M., Ichikawa T., Gunn J. E., Doi M., Shimasaku K., Schneider D. P., 1996, AJ, 111, 1748
Gunn J. E. et al., 1998, AJ, 116, 3040
Hogg D. W., Finkbeiner D. P., Schlegel D. J., Gunn J. E., 2001, AJ, 122, 2129
Hogg D. W., Baldry I. K., Blanton M. R., Eisenstein D. J., 2002, preprint (astro-ph/0210394)
Hopkins A. M., 2004, ApJ, 615, 209
Hopkins A. M., Connolly A. J., Haarsma D. B., Cram L. E., 2001, AJ, 122, 288
Hopkins A. M., Miller C. J., Nichol R. C. et al., 2003, ApJ, 599, 971
Ilbert O. et al., 2004, A&A, submitted (astro-ph/0409134)
Jones D. H. et al., 2004, MNRAS, 355, 747
Le Fèvre O. et al., 2004, A&A, submitted (astro-ph/0409133)
Lilly S. J., Le Fevre O., Hammer F., Crampton D., 1996, ApJ, 460, L1
Lin H., Yee H. K. C., Carlberg R. G., Morris S. L., Sawicki M., Patton D. R., Wirth G., Shepherd C. W., 1999, ApJ, 518, 533
Lupton R. H., Gunn J. E., Szalay A. S., 1999, AJ, 118, 1406
Lupton R. H., Gunn J. E., Ivezić Z., Knapp G. R., Kent S., Yasuda N., 2001, in Harnden F. R., Primini F. A., Payne H. E., eds, ASP Conf. Ser. Vol. 238, Astronomical Data Analysis Software Systems X. Astron. Soc. Pac., San Francisco, p. 269
Madau P., Ferguson H. C., Dickinson M. E., Giavalisco M., Steidel C. C., Fruchter A., 1996, MNRAS, 283, 1388
Madau P., Pozzetti L., Dickinson M., 1998, ApJ, 498, 106
Martin C. et al., 2003, Proc. SPIE, 4854, 336
Martin D. C. et al., 2005, ApJ, 619, L1
Milliard B., Donas J., Laget M., Armand C., Vuillemin A., 1992, A&A, 257, 24
Oke J. B., Gunn J. E., 1983, ApJ, 266, 713
Percival W. J. et al., 2001, MNRAS, 327, 1297
Petrosian V., 1976, ApJ, 209, L1
Pier J. R., Munn J. A., Hindsley R. B., Hennessy G. S., Kent S. M., Lupton R. H., Ivezić Ž., 2003, AJ, 125, 1559
Richards G. T. et al., 2002, AJ, 123, 2945
Schechter P., 1976, ApJ, 203, 297
Schiminovich D. et al., 2005, ApJ, 619, L47
Schlegel D. J., Finkbeiner D. P., Davis M., 1998, ApJ, 500, 525
Schmidt M., 1968, ApJ, 151, 393
Smith J. A. et al., 2002, AJ, 123, 2121
Somerville R. S., Lee K., Ferguson H. C., Gardner J. P., Moustakas L. A., Giavalisco M., 2004, ApJ, 600, L171
Steidel C. C., Adelberger K. L., Giavalisco M., Dickinson M., Pettini M., 1999, ApJ, 519, 1
Stoughton C. et al., 2002, AJ, 123, 485
Strateva I. et al., 2001, AJ, 122, 1861
Strauss M. A. et al., 2002, AJ, 124, 1810
Sullivan M., Treyer M. A., Ellis R. S., Bridges T. J., Milliard B., Donas J., 2000, MNRAS, 312, 442

Treyer M. A., Ellis R. S., Milliard B., Donas J., Bridges T. J., 1998, MNRAS, 300, 303

Uomoto A. et al., 1999, Bull. Am. Astron. Soc., 31, 1501

Vanden Berk D. et al., 2005, AJ, 129, in press (astro-ph/0501113)

Wilson G., Cowie L. L., Barger A. J., Burke D. J., 2002, AJ, 124, 1258

Wolf C., Meisenheimer K., Rix H.-W., Borch A., Dye S., Kleinheinrich M., 2003, A&A, 401, 73

Wyder T. K. et al., 2005, ApJ, 619, L15

York D. G. et al., 2000, AJ, 120, 1579

APPENDIX A: MORE DETAILS ON THE LUMINOSITY FUNCTIONS

We use a straightforward V_{max} in slices approach for determining the LFs (Section 4). Schechter functions are fitted to the LFs using standard least-squares routines. The errors on each 0.2-mag bin are taken to be a modified Poisson error where the variance without weighting would be $N + 2$. This is an appropriate variance for low number counts (when the expected value is not known). Fig. A1 shows the best-fitting faint-end slopes versus redshift. As there are significant degeneracies between M^* and α, we considered a limited range in α, -1.15 to -0.95, in order to assess the evolution in M^* and ϕ^*. Table A1 gives the Schechter parameters for the redshift slices along with some details of the LF fitting.

The top half of Table A1 gives the absolute magnitude ranges used in the fitting, the number of galaxies, the mean of the correction factors and the Schechter parameters for α marginalized over the range -1.15 to -0.95. The column $1/f_{j,\mathrm{obs}}$ gives the 1σ range (not including cosmic variance) of the inverse of the fraction of LD that is within the magnitude limits, i.e. it represents the extrapolation factor from the observed to total LD. The ϕ^* and j errors include an estimate of cosmic variance, that is proportional to $V^{-0.3}$, added in quadrature to the Poisson errors. This approximate power and the normalization were estimated from fig. 3 of Somerville et al. (2004). The cosmic variance on j is assumed to be less than that
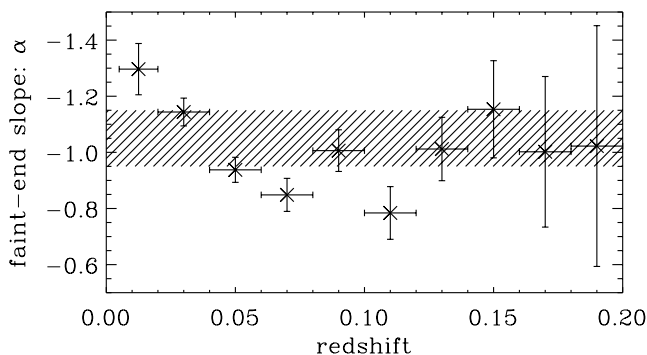

Figure A1. Best-fitting faint-end slopes for the $^{0.1}u$ LFs. The horizontal bars represent the redshift ranges while the vertical error bars represent the 1σ errors. The sloped-line region shows the allowed α range when fitting the other Schechter parameters. Note that we do not interpret the change in α from $z = 0.0$ to 0.1 as being caused by galaxy evolution. The change could be caused by the varying magnitude limits in the fitting (Table A1). For the lowest redshift slices there is a higher weight from luminosities fainter than $\sim M^* + 1$; whereas at $z \sim 0.05$–0.1 the fitting is giving higher weight to the 'knee' of the LF. In other words, the Schechter function is not a perfect match to the LF as there appears to be a change in slope around $M_{322} \sim -16.5$ (Fig. 7). For the purposes of this paper, assessing the evolution in M^* and j, we use the three-parameter Schechter function and compromise on α. Note also there could be systematic errors at low redshift because of deblending issues that increase the number of faint galaxies at the expense of bright galaxies.

on ϕ^* because the specific SFR per galaxy increases in low-density environments, which partly offsets changes in number density.

The lower half of Table A1 gives the Schechter parameters for fixed $\alpha = -1.05$ for both the $^{0.1}u$ and the ^0u band. From the M^* and j differences between the different bands, we obtain

$$M_{355} \approx M_{322} - 0.35 \qquad (A1)$$

for the average galaxy, which is in good agreement with that determined from the cosmic spectrum fit (Fig. 10).

We provide these Schechter parameters to make comparisons with other surveys but they are strictly only valid from about $M^* - 2.5$ (or the bright limit) to the faint limit of the fitting. At magnitudes brighter than about $M^* - 2.5$, there is a significant excess of galaxies above the Schechter fit (from a composite LF with each redshift slice shifted by M^*).

APPENDIX B: SKY-SUBTRACTION CORRECTIONS FOR SDSS U-BAND PETROSIAN FLUXES

The equivalent depths across the SDSS magnitudes for galaxy target selection correspond to $(u, g, r, i, z) \approx (19.8, 18.6, 17.8, 17.4, 17.1)$. In other words, there are an equivalent number of galaxies per square degree ($\sim 100\,\mathrm{deg}^{-2}$) for galaxies brighter than these limits in each of the bands. These also approximately correspond to the average spectral energy distribution of galaxies near those magnitudes. Comparing these limits (plus average MW extinction) to the point source 95 per cent completeness limits given in Stoughton et al. (2002), we obtain differences of (1.9, 3.4, 4.2, 3.8, 3.3). Thus, the u-band galaxy measurements are, on average, the closest to the survey imaging detection limit. In addition, systematic errors can dominate because scattered light can be significant in comparison with the sky flux (which is less of a problem in the z band, for example). This can affect flat fielding and the zero point of the sky-subtracted frame and therefore is most significant for galaxies with low SBs. The distribution of u-band SBs in the Petrosian aperture ($2\times$ the Petrosian radius in the r band) is shown in Fig. B1 for a galaxy sample.

The variation of the average u–g galaxy colour, as a function of camera column, is shown in Fig. B2 for different SB bins. There is a significant non-astrophysical variation of the average colour and the amplitude of the variation increases with decreasing SB. The variation is reduced by using model colours because the effective aperture is smaller. The peak-to-peak systematic variation of u–g colour is around 0.3–0.4 for Petrosian magnitudes (lower two panels of Fig. B2) and around 0.1–0.2 for model magnitudes, for galaxies with u-band SBs between 27 and 28 mag arcsec^{-2}.

On the assumption that the dominate systematic error is owing to sky-subtraction errors, we determined linear offsets in SB as a function of pixel position that minimized the colour variation. This was done by using the three lowest SB bins and fitting a cubic polynomial to the implied offsets for each camera column separately. The u_{petro} fluxes were redetermined and the process was iterated until the results converged. The mean flux offset was normalized to zero. The polynomial coefficients are given in Table B1 and should be applied so that

$$u'_{\mathrm{flux}} = u_{\mathrm{flux}} + P(\mathrm{objc\_colc})\,\pi\,(2R_r)^2 \qquad (B1)$$

where u_{flux} is the pipeline Petrosian flux in units of 'maggies' [$-2.5 \log(\mathrm{maggies}) = \mathrm{mag}$], P is the polynomial function of the pixel position, which is different for each 'camcol' and R_r is the Petrosian radius in the r band. Note that the SDSS databases use

Table A1. Luminosity function fitting and Schechter parameters [a]

Range of z	M_{322} limits bright	M_{322} limits faint	No. of galaxies	Mean of $1/C$	Mean of V_{slice}/V_{max}	M_{322} parameters marginalized over $\alpha = -1.05 \pm 0.10$ $-M^*$	$-\log \phi^*$	$-j$	$1/f_{j,obs}$
0.005–0.02	−18.6	−14.4	601	1.07	1.01	$<18.58^b$	2.05 ± 0.15	13.44 ± 0.28	1.32–1.55
0.02–0.04	−20.0	−15.4	2421	1.17	1.01	18.61 ± 0.09	2.10 ± 0.09	13.46 ± 0.15	1.06–1.14
0.04–0.06	−21.4	−16.4	4738	1.15	1.01	18.64 ± 0.04	1.96 ± 0.06	13.73 ± 0.11	1.09–1.13
0.06–0.08	−21.4	−17.0	5334	1.23	1.01	18.75 ± 0.02	2.03 ± 0.05	13.64 ± 0.09	1.17–1.21
0.08–0.10	−21.6	−17.6	5058	1.25	1.01	18.84 ± 0.06	2.12 ± 0.05	13.55 ± 0.09	1.33–1.42
0.10–0.12	−21.6	−18.0	5143	1.34	1.03	18.88 ± 0.02	2.10 ± 0.04	13.60 ± 0.07	1.46–1.51
0.12–0.14	−21.8	−18.4	5549	1.47	1.04	18.90 ± 0.06	1.99 ± 0.04	13.95 ± 0.09	1.81–2.05
0.14–0.16	−22.0	−18.8	3549	1.51	1.04	19.03 ± 0.06	2.15 ± 0.04	13.74 ± 0.11	2.25–2.64
0.16–0.18	−22.2	−19.2	2719	1.49	1.06	19.06 ± 0.07	2.11 ± 0.04	13.82 ± 0.14	2.95–3.74
0.18–0.20	−22.2	−19.6	1987	1.48	1.03	19.13 ± 0.07	2.07 ± 0.05	13.99 ± 0.17	4.35–5.85
0.20–0.22	−22.2	−19.8	1259	1.74	1.06	19.17 ± 0.06	2.12 ± 0.05	13.92 ± 0.19	5.46–7.62
0.22–0.24	−22.4	−20.2	467	1.71	1.04	19.16 ± 0.08	$>2.02^c$	13.90 ± 0.29	11.7–19.7
0.24–0.26	−22.4	−20.4	313	1.92	1.07	19.27 ± 0.06	$>2.09^c$	13.92 ± 0.22	16.0–24.0
0.26–0.28	−22.4	−20.6	220	2.17	1.04	19.36 ± 0.06	$>2.10^c$	13.99 ± 0.21	21.4–31.4
0.28–0.30	−22.4	−20.8	136	2.17	1.18	19.44 ± 0.07	$>2.05^c$	14.12 ± 0.27	29.6–47.9

Range of z	M_{322} parameters with fixed $\alpha = -1.05$ $-M^*$	$-\log \phi^*$	$-j$	$1/f_{j,obs}$	M_{355} parameters with fixed $\alpha = -1.05^d$ $-M^*$	$-\log \phi^*$	$-j$	$1/f_{j,obs}$
0.005–0.02	$<18.45^b$	1.96 ± 0.15	13.53 ± 0.27	1.50–1.64	$<18.86^b$	2.00 ± 0.15	13.85 ± 0.27	1.44–1.58
0.02–0.04	18.47 ± 0.05	2.02 ± 0.08	13.44 ± 0.15	1.04–1.11	18.88 ± 0.05	2.06 ± 0.08	13.76 ± 0.15	1.04–1.11
0.04–0.06	18.76 ± 0.03	2.02 ± 0.06	13.75 ± 0.11	1.11–1.15	19.16 ± 0.03	2.04 ± 0.06	14.08 ± 0.11	1.08–1.11
0.06–0.08	18.85 ± 0.02	2.08 ± 0.05	13.67 ± 0.09	1.20–1.24	19.25 ± 0.02	2.12 ± 0.05	13.99 ± 0.09	1.20–1.24
0.08–0.10	18.87 ± 0.02	2.14 ± 0.05	13.57 ± 0.08	1.38–1.42	19.26 ± 0.02	2.16 ± 0.05	13.88 ± 0.08	1.39–1.43
0.10–0.12	18.95 ± 0.02	2.13 ± 0.04	13.65 ± 0.07	1.54–1.58	19.32 ± 0.02	2.15 ± 0.04	13.98 ± 0.07	1.56–1.60
0.12–0.14	18.91 ± 0.02	2.00 ± 0.04	13.96 ± 0.07	1.91–1.98	19.28 ± 0.02	2.01 ± 0.04	14.28 ± 0.07	1.96–2.02
0.14–0.16	19.01 ± 0.02	2.13 ± 0.04	13.71 ± 0.06	2.32–2.43	19.40 ± 0.02	2.17 ± 0.04	14.01 ± 0.06	2.36–2.48
0.16–0.18	19.06 ± 0.03	2.11 ± 0.04	13.81 ± 0.07	3.19–3.41	19.40 ± 0.03	2.10 ± 0.04	14.18 ± 0.07	4.30–4.70
0.18–0.20	19.13 ± 0.03	2.07 ± 0.04	13.98 ± 0.08	4.76–5.27	19.43 ± 0.04	2.02 ± 0.05	14.42 ± 0.09	7.57–8.73

[a] See text of Appendix A for details. The units of M^*, ϕ^* and j are AB mag, Mpc^{-3} and AB mag Mpc^{-3}, respectively. [b] The M^* limits shown for the lowest redshift slice are 1σ limits when M^* is constrained to be brighter than -18.4 and -18.8 for 322 and 355 nm, respectively. [c] The ϕ^* limits for the redshift slices above 0.22 are 1σ limits when $\log \phi^*$ is constrained to be greater than -2.2. [d] The faint M_{355} limits for the fitting were $(-0.2, -0.4, -0.6)$, with respect to the M_{322} limits, for the redshift ranges $(0–0.06, 0.06–0.16, 0.16–0.20)$, respectively. The bright M_{355} limits were -0.2 or -0.4 with respect to the M_{322} limits. Beyond $z = 0.2$, the ^0u LFs are significantly less reliable because of V_{max} and k corrections, and a g-based sample would be more appropriate.
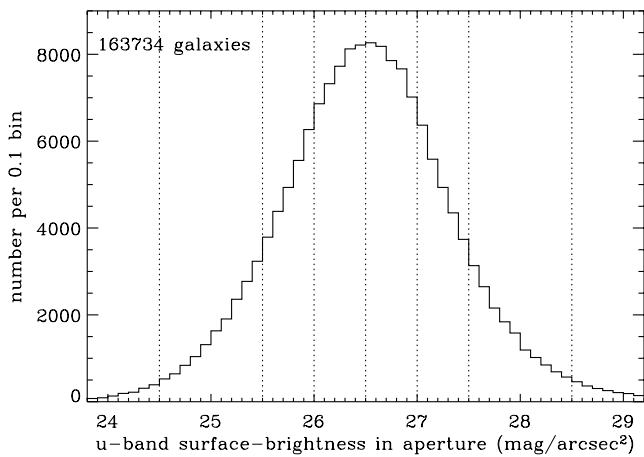

Figure B1. Distribution of u-band SBs for a galaxy sample with $r_{petro} < 19.4$. The vertical dotted lines show the positions of the cuts used to divide the sample for testing. Note that the SBs are for the SDSS Petrosian aperture, which is two times the Petrosian radius in the r band, and the values have not been corrected for MW extinction (unlike all other flux measurements in this paper).

asinh magnitudes (Lupton et al. 1999), which can be converted to flux by

$$X_{flux} = \sinh\left[-\frac{\ln(10)}{2.5}X_{mag} - \ln(b)\right] 2b \qquad (B2)$$

where the b values are $(1.4, 0.9, 1.2, 1.8, 7.4) \times 10^{-10}$ for *ugriz*, respectively (Stoughton et al. 2002).

Table B1. Polynomial coefficients for the u-band Petrosian flux corrections as a function of objc_colc.

camcol	$p_0/10^{-12}$	$p_1/10^{-15}$	$p_2/10^{-18}$	$p_3/10^{-21}$
1	0.187	−2.976	3.767	−1.101
2	0.902	5.103	−6.910	2.063
3	−0.616	−1.674	2.391	−0.749
4	0.485	−1.027	1.460	−0.456
5	0.481	−6.971	7.650	−2.181
6	0.242	−1.933	2.514	−0.907

See equations (B1)–(B2) for how to apply the correction, and see Fig. B3 for an illustration of the offsets for each of the camera columns. Note that these corrections were determined for PHOTO v. 5.4 and a Southern Survey co-added catalogue. Similar offsets are observed using earlier versions of the pipeline and for different regions of the sky.
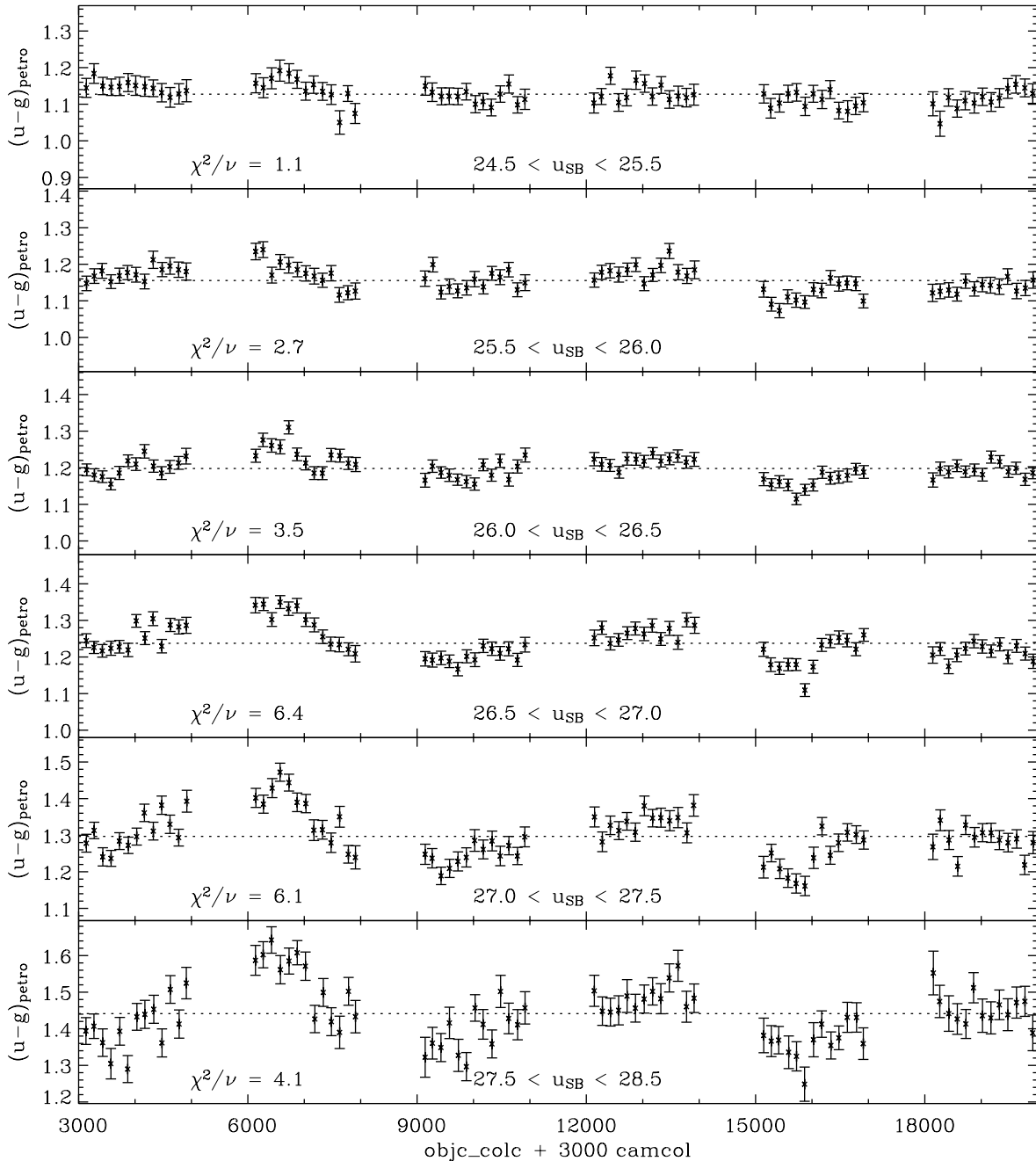
Figure B2. Variation in the average observed *u–g* galaxy colours as a function of the pixel position ('objc_colc') and the camera column ('camcol'). The panels represent different SB bins. The reduced χ^2 values on the assumption of no variation with camera position are shown in the panels, with the dotted lines showing the mean colour. Note that the SDSS cameras operate in drift-scan mode so that any systematic error only depends on the detector column (and not on the detector row).

A plot of the offsets is shown in Fig. B3 and the variation in the *u–g* colour after correction is shown in Fig. B4. After correction, there is no significant variation with camera column for each SB bin (reduced $\chi^2 \sim 1$). This implies that our assumption that sky subtraction was the dominate systematic error varying with camera column was valid. For galaxies with low SBs (28 mag arcsec^{-2} over the aperture), the correction can be up to ± 0.3 mag depending on the pixel position.
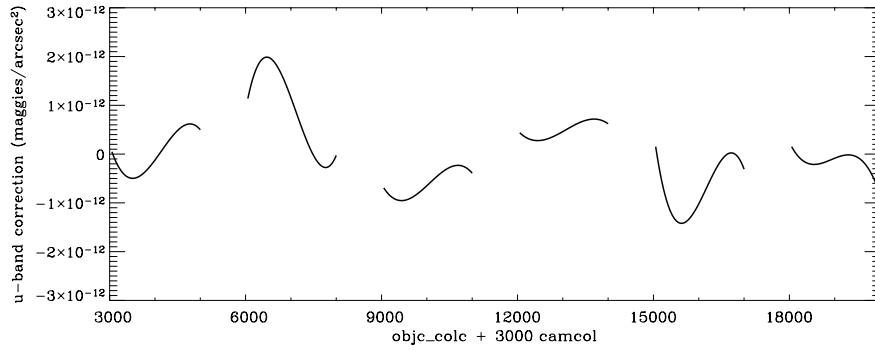
Figure B3. Estimated flux offsets required to correct sky-subtraction errors in the *u* band. The lines represent the polynomial fits to the data given in Table B1. The units are linear in flux where 10^{-12} maggies corresponds to a magnitude of 30 [i.e. $-2.5 \log(\text{maggies}) = \text{mag}$]. The average of the flux offsets was normalized to zero. Note that these offsets were determined using a Southern Survey co-added catalogue where there was some smoothing over objc_colc (FWHM $\sim$ 50–200) because some drift-scan runs were offset slightly in Dec.
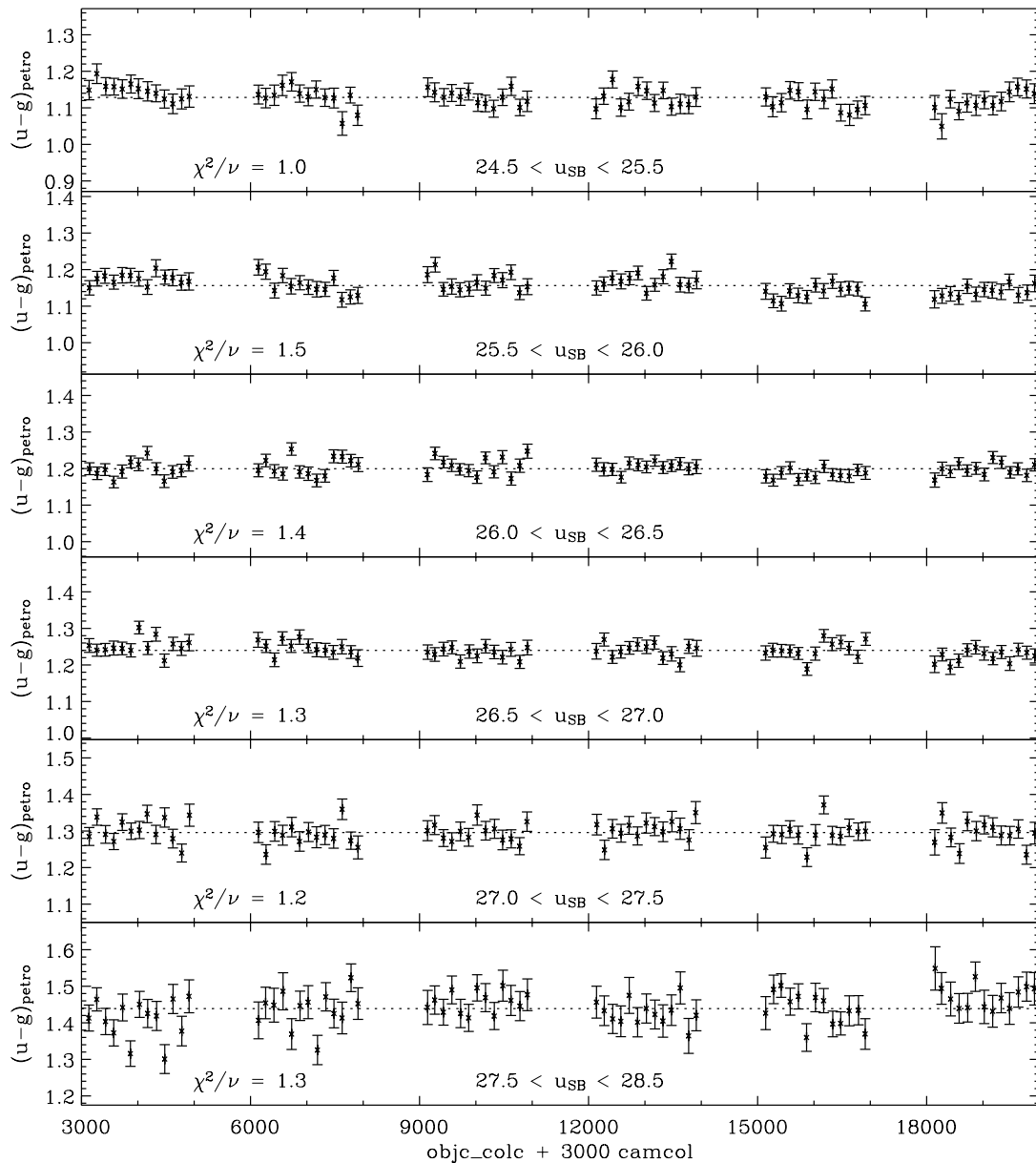

Figure B4. Same as Fig. B2 except the *u*-band fluxes have been corrected using the functions given in Table B1.

This paper has been typeset from a TEX/LATEX file prepared by the author.